

Closure Relations for Shallow Granular Flows from Particle Simulations

Thomas Weinhart^{1,2} · Anthony Thornton^{1,2,†} · Stefan Luding¹ · Onno Bokhove²

Received: date / Accepted: date

Abstract The Discrete Particle Method (DPM) is used to model granular flows down an inclined chute with varying basal roughness, thickness and inclination. We observe three major regimes: arresting flows, steady uniform flows and accelerating flows. For flows over a smooth base, other (quasi-steady) regimes are observed: for small inclinations the flow can be highly energetic and strongly layered in depth; whereas, for large inclinations it can be non-uniform and oscillating.

For steady uniform flows, depth profiles of density, velocity and stress are obtained using an improved coarse-graining method, which provides accurate statistics even at the base of the flow. A shallow-layer model for granular flows is completed with macro-scale closure relations obtained from micro-scale DPM simulations of steady flows. We obtain functional relations for effective basal friction, shape factor, mean density, and the normal stress anisotropy as functions of layer thickness, flow velocity and basal roughness.

Keywords Discrete Particle Method · Coarse graining · Granular chute flow · Depth-averaging · Shallow-layer equations

1 General introduction

1.1 Background

Granular avalanche flows are common in both the natural environments and industry. They occur across many orders

of magnitude. Examples range from rock slides, containing upwards of 1000m^3 of material; to the flow of sinter, pellets and coke into a blast furnace for iron-ore melting; down to the flow of sand in an hour-glass. The dynamics of these flows are influenced by many factors such as: polydispersity; variations in density; non-uniform shape; complex basal topography; surface contact properties; coexistence of static, steady and accelerating material; and, flow obstacles and constrictions.

Discrete Particle Methods (DPMs) are an extremely powerful way to investigate the effects of these and other factors. With the rapid recent improvement in computational power the full simulation of the flow in a small hour glass of millions of particles is now feasible. However, complete DPM simulations of large-scale geophysical mass flow will, probably, never be possible.

One of the main goals of the present research is to simulate large scale and complex industrial flows using granular shallow-layer equations. In this paper we will take the first step of using the DPM [CS79, SEG⁺01, SGPL02, SLG03, Lud08] to simulate small granular flows of mono-dispersed spherical particles in steady flow situations. We will use a refined and novel analysis to investigate three particular aspects of shallow chute flows: *i*) how to obtain meaningful macro-scale fields from the DPM simulation, *ii*) how to assess the flow dependence on the basal roughness, and *iii*) how to validate the assumptions made in depth-averaged theory.

The DPM simulations presented here will enable the construction of the mapping between the micro-scale and macro-scale variables and functions, thus enabling construction of a closed set of continuum equations. These mappings (closure relations) can then be used in continuum shallow-layer models and compared with full DPM simulations (DPMs). For certain situations, precomputed closures should work; but, in very complicated situations pre-established relations

¹ Dept. of Mechanical Engineering, Univ. of Twente, The Netherlands

² Dept. of Applied Mathematics, Univ. of Twente, The Netherlands Mathematics of Computational Science group and MultiScale Mechanics group, University of Twente, P.O. Box 217, 7500 AE Enschede, The Netherlands, Tel.: +31 53 489 3301, Fax: +31 53 489 4833, E-mail: {t.weinhart, a.r.thornton[†], s.luding, o.bokhove}@utwente.nl

may fail. Heterogeneous, multi-scale modelling (HMM) is then an alternative [WEL⁺07], in which the local constitutive relations are directly used in the continuum model. In HMM, continuum and micro-scale models are dynamically coupled with a two-way communication between the different models in selective regions in both space and time, thus reducing computational expense and allowing simulation of complex granular flows.

1.2 Shallow-layer models

Shallow-layer granular continuum models are often used to simulate geophysical mass flows, including snow avalanches [CGJ07], dense pyroclastic flows, debris flows [DI01], block and ash flows [DPP⁺08] and lahars [WSS08]. Such shallow-layer models involve approximations reducing the properties of a huge number of individual particles to a handful of averaged quantities. Originally these models were derived from the general continuum incompressible mass and momentum equations, using the long-wave approximation [SH89, HSSN93, GWH99, WGH99, GTN03, BT12] for shallow variations in the flow height and basal topography. Despite the massive reduction in degrees of freedom made, shallow-layer models tend to be surprisingly accurate, and are thus an effective tool in modelling geophysical flows. Moreover, they are now used as a geological risk assessment and hazard planning tool [DPP⁺08]. In addition to these geological applications, shallow granular equations have been applied to analyse small-scale laboratory chute flows containing obstacles [GTN03], wedges [HH05, GC07] and contractions [VATK⁺07], showing good quantitative agreement between theory and experiment.

In fluid dynamics, the Navier-Stokes equations are established with full constitutive equations. Nonetheless, the shallow-layer equations or Saint-Venant equations are often used in large scale situations where it is impractical to solve the full Navier-Stokes equations. Our present aim is to directly investigate the validity of the assumptions of granular shallow-layer models first from discrete particle simulations, before obtaining fully 3D ‘kinetic theory’-style constitutive relations and simplifying these via the depth-integration process. A discussion of the full three-dimensional properties of our particle simulations will be undertaken later. Here we restrict our attention to the closures required for two-dimensional shallow-layer granular flow equations.

A key difference between shallow-layer fluid models and granular ones is the appearance of a basal friction coefficient, μ , being the ratio of the shear to normal traction at the base. In early granular models, a dry Coulomb-like friction law was used [SH89]. It implies μ to be constant, given by the tangent of the friction angle between the material and the base, δ , *i.e.*, $\mu = \tan \delta$. As a consequence constant uniform

flow is only possible in such a model at the angle δ , independent of height. There is a considerable amount of experimental evidence, *e.g.*, [DD99, GDR04], that suggests that such a simple Coulomb law does not hold on rough beds or for moderate inclination angles. Furthermore, detailed experimental investigations using glass beads [Pou99] lead to an improved empirical ‘Pouliquen’ friction law characterised by two angles: the angle at which the material comes to rest, δ_1 , below which friction dominates over gravity and the angle, δ_2 , above which gravity dominates over friction and the material accelerates. Between these two angles steady flow is possible, and in the limit $\delta_1 \rightarrow \delta_2 = \delta$ the original Coulomb style model is recovered.

Since its formulation a lot of work has been performed on extending and understanding this Pouliquen law. The original law was obtained by retarding flowing material and measuring the angle at which the material stopped as a function of height $h_{stop}(\theta)$, or equivalently, by inverting this relation, $\theta_{stop}(h)$. For most materials, granular included, a greater angle is required to initiate stationary than to retard flowing material. Pouliquen and Forterre [PF02], by measuring the angle required to start motion, measured $\theta_{start}(h)$, *i.e.*, the friction law for initially stationary material. As expected θ_{start} was greater than θ_{stop} and this information was used to extend the friction law to all values of the height and velocity within the steady regime. Borzsonyi & Ecke performed a series of additional experiments: firstly, in [BE06] they looked at higher angles where the mean flow rates are close to the terminal velocity of a single particle, and found regions where the Pouliquen law is not valid and the Froude number becomes inversely proportional to the height, as opposed to the linear relationship observed for steady flow. Borzsonyi and Ecke, and Pouliquen and Forterre [BE07, FP03] have all worked on extending the original law to be valid for more complicated non-spherical materials like sand and metallic materials. Also, the effect of basal surface roughness has been systemically studied in [GTDD03] by varying the size of both the free flow and fixed basal particles. For convenience, we define λ to be the size ratio of the fixed and the free particles. They observed a peak in roughness at a certain diameter ratio, λ_c , which depends on the compactness of the basal layer. Measured values of λ_c in [GTDD03] ranged between 1 and 3 for a monolayer of fixed particles. For fixed particles with smaller size and $\lambda < \lambda_c$, the range of angles where steady flow was observed decreased, and eventually the steady flow regime completely vanished, *i.e.*, $\delta_2 - \delta_1 \rightarrow 0$ as $\lambda \rightarrow 0$ (yielding Coulomb type behaviour). For smaller flow particle diameters, *i.e.*, with $\lambda > \lambda_c$, there was also a reduction in friction, but weaker than in the small λ case. For much larger λ , the friction saturated to a constant value, which they contributed to free particles that filled the holes in the basal surface and effectively created a stable basal surface of free particles. In a

later publication [GDDT07], they extended this investigation to flows containing two particle sizes.

Louge and Keast [LK01] modified the kinetic theory presented in [Jen93] by modelling enduring contacts via a frictional rate-independent stress component in order to obtain steady flow on flat frictional inclines. This work was later extended to bumpy inclines [Lou03]. Jenkins [Jen06] took a different approach and theoretically formulated a phenomenological modification of granular kinetic theory to account for enduring particle contacts. His idea is that enduring contacts between grains, forced by the shearing, reduce the collision rate of dissipation. Therefore a modification to the dissipation is introduced, which does not affect the stress. It leads to a law very similar to the one experimentally obtained by Pouliquen. Jenkins further extended the theory in [Jen07] to very dissipative frictional particles, with a coefficient of restitution less than 0.7. Later, a detailed comparison with new experiments was performed, showing agreement for flows on low inclinations [JB10].

Silbert *et al.* [SEG⁺01] used DPMs to simulate chute flow of cohesionless particles. They found that a steady-state flow regime exists over a wide range of inclination angles, heights and interaction parameters, in confirmation of the experiments of Pouliquen [Pou99]. They found for steady-state flows that the volume fraction is constant throughout the flow, in agreement with the assumptions of shallow-layer theory [SH89]. They also observed that the shear stress is proportional to the square of the shear and the flow velocity scales with the height to the power $3/2$. This result coincides with Bagnold's analysis of dilute binary collisions flows [Bag54]. They also observed small systematic deviations from isotropic stress, which shows a deviation from fluid-like behaviour. However, normal stresses do not approach a Coulomb-yield criterion structure at the angle of repose except near the surface, hinting that the failure of flow starts near the surface. They further investigated the effect of different basal types in [SGPL02] and found that for an ordered chute base the steady state regime splits into three distinct flow regimes: at smaller angles, the flowing system self-organises into a state of low-dissipation flow consisting of in-plane ordering in the bulk; at higher angles, a high-dissipation regime similar to that for a rough base but with considerable slip at the bottom is observed; and, between these two sub-regions they observe a transitional flow regime characterised by large oscillations in the bulk averaged kinetic energy due to the spontaneous ordering and disordering of the system as a function of time. In [TRJD07], a strongly sheared, dilute and agitated basal layer could be observed supporting a compact bulk layer over a relatively smooth base. They essentially concluded for transitional flows that a steady and thus unstable state could only be reached at one inclination. Finally, [SLG03] investigated the initiation and cessation of granular chute flow more care-

fully and computed both θ_{stop} and θ_{start} . For inclinations $\theta \gg \theta_{stop}$ they observed a Bagnold rheology, for $\theta \gtrsim \theta_{stop}$ a linear profile, and for $\theta \approx \theta_{stop}$ intermittent flow.

1.3 Overview of this study

Our present research is novel on the following three counts:

Firstly, we compute more meaningful macro-scale fields from the DPM simulations than before by carefully choosing the coarse graining function. In order to homogenise the DPM data, the micro-scale fields need to be coarse-grained to obtain macroscopic fields. Coarse-grained micro-scale fields of density, momentum and stress have been derived directly from the mass and momentum balance equations, e.g., by Goldhirsch [Gol10]. The quality of the statistics involved depends on the coarse graining width w , which defines the amount of spatial smoothing. For small coarse-graining width w , micro-scale variations remain visible, while for large w these smooth out in the macro-scale gradients. Since one of the objectives is to obtain the value of μ at the base, we use a novel adaptation of Goldhirsch' statistics near boundaries. This new approach [WTLB11] is consistent with the continuum equations everywhere, enabling the construction of continuum fields even within one coarse-graining width of the boundary.

Secondly, we follow the approach of [GTDD03] and vary the basal particle diameter to achieve different basal conditions. For particles with smaller basal than flowing diameter, $\lambda < 1$, the flow becomes more energetic and oscillatory behaviour is observed. This phenomena has previously been reported in [SGPL02], but was achieved by changing the basal particles to a more regular, grid-like configuration. By investigating flow over fixed particles of different size than the free, flowing particles, we are able to quantify the roughness and numerically investigate the transition from rough to smooth surfaces. For smoother surfaces, we show that the parameter space can be split into two types of steady flow, and we obtain a general friction law.

Finally, we test the assumptions made in depth-averaged theory and determine the required closure laws. For shallow granular flows, the flow can be described by depth-averaged mass and momentum-balance equations [GTN03]. Solving the depth-averaged equations requires a constitutive relation for the basal friction, a way to account for mean density variations, the shape of the velocity profile and the pressure anisotropy. We extract such data from DPMs obtained for steady uniform flows, and establish a novel, extended set of closure equations. Also, the depth-averaged equations are obtained under the assumptions that a) the density is constant in space and time and does not vary through the flow; b) the ratio between mean squared velocity and the squared mean velocity is known; c) the downward normal

stress is lithostatic, *i.e.*, balances the gravitational forces acting on the flow; and, d) the ratio between the normal stresses is known. Gray *et al.* [GTN03] assumed the latter ratio to be one, whereas Savage and Hutter [SH89] use a Mohr-Coulomb closure law. The depth profiles of these quantities are discussed by Silbert *et al.* in [SEG⁺01, SGPL02, SLG03] for steady flow. We used the originally results of Silbert *et al.* to validate our DPM simulations. Then, using our improved statistical procedure, we will construct the granular shallow-layer closer relations for a much wider range of flow regimes than had been considered before; concurrently, establishing the range in which the shallow-layer approximation is valid.

1.4 Outline

We introduce the force model used in the DPM in Sect. 2, and the statistical method used to obtain macroscopic density, velocity and stress profiles in Sect. 3. In Sect. 4, we discuss the continuum shallow-layer equations for modelling granular flow including some macro-scale closures. The set up of the simulations is discussed in Sect. 5, and the steady-state regime is mapped for flows over a rough basal surface in Sect. 6. Depth profiles of the flow are introduced in Sect. 7, which are then used to characterise the steady flow over smoother surfaces in Sect. 8. Finally, the closure relations for the shallow-layer model are established in Sect. 9, before we conclude in Sect. 10.

2 Contact law description

A Discrete Particle Method (DPM) is used to perform the simulation of a collection of N identical granular particles. Boundaries are created by special fixed particles, which generally will have different properties than the flow particles. Particles interact by the standard spring-dashpot interaction model [CS79, WB86, Lud08], in which it is assumed that particles are spherical and soft, and that pairs have at most a single contact point.

Each particle i has a diameter d_i , density ρ_i , position \mathbf{r}_i , velocity \mathbf{v}_i and angular velocity $\boldsymbol{\omega}_i$. For pairs of two particles $\{i, j\}$, we define the relative distance vector $\mathbf{r}_{ij} = \mathbf{r}_i - \mathbf{r}_j$, their separation $r_{ij} = |\mathbf{r}_{ij}|$, the unit normal $\hat{\mathbf{n}}_{ij} = \mathbf{r}_{ij}/r_{ij}$ and the relative velocity $\mathbf{v}_{ij} = \mathbf{v}_i - \mathbf{v}_j$. Two particles are in contact if their overlap,

$$\delta_{ij}^n = \max(0, (d_i + d_j)/2 - r_{ij}), \quad (1)$$

is positive. A single contact point \mathbf{c} at the centre of the overlap is assumed, which is a valid assumption as long as the overlap is small. For our simulations the overlap between two particles is always below 1% of the particle radius, hence justifying treating the contact as occurring at a single point.

The force acting on particle i is a combination of the body forces and the pairwise interaction of two particles. The force \mathbf{f}_{ij} represents the force on particle i from the interaction with particle j and can be decomposed into a normal and a tangential component,

$$\mathbf{f}_{ij} = \mathbf{f}_{ij}^n + \mathbf{f}_{ij}^t. \quad (2)$$

We assume particles experience elastic as well as dissipative forces in both normal and tangential directions. Hence the normal force is modelled as a spring-dashpot with a linear elastic and a linear dissipative contribution,

$$\mathbf{f}_{ij}^n = k^n \delta_{ij}^n \hat{\mathbf{n}}_{ij} - \gamma^n \mathbf{v}_{ij}^n, \quad (3)$$

with spring constant k^n , damping coefficient γ^n and the normal relative velocity component,

$$\mathbf{v}_{ij}^n = (\mathbf{v}_{ij} \cdot \hat{\mathbf{n}}_{ij}) \hat{\mathbf{n}}_{ij}. \quad (4)$$

For a central collision, no tangential forces are present, and the collision time t_c between two particles can be calculated as

$$t_c = \pi / \sqrt{\frac{k^n}{m_{ij}} - \left(\frac{\gamma^n}{2m_{ij}}\right)^2}, \quad (5)$$

with the reduced mass $m_{ij} = m_i m_j / (m_i + m_j)$. The normal restitution coefficient r_c (ratio of relative normal speed after and before collision) is calculated as

$$r_c = \exp(-t_c \gamma^n / (2m_{ij})). \quad (6)$$

We also assume a linear elastic and a linear dissipative force in the tangential direction,

$$\mathbf{f}_{ij}^t = -k^t \boldsymbol{\delta}_{ij}^t - \gamma^t \mathbf{v}_{ij}^t, \quad (7)$$

with spring constant k^t , damping coefficient γ^t , elastic tangential displacement $\boldsymbol{\delta}_{ij}^t$ (which is explained later), and total relative velocity of the particle surfaces at the contact,

$$\mathbf{v}_{ij}^t = \mathbf{v}_{ij} - \mathbf{v}_{ij}^n + \mathbf{b}_{ij} \times \boldsymbol{\omega}_i - \mathbf{b}_{ji} \times \boldsymbol{\omega}_j, \quad (8)$$

with $\mathbf{b}_{ij} = -((d_i - \delta_{ij}^n)/2) \hat{\mathbf{n}}_{ij}$ the branch vector from point i to the contact point; for equal size particles $\mathbf{b}_{ij} = -\mathbf{r}_{ij}/2$.

The elastic tangential force is used to model the effects of particle surface roughness. Near the contact point, small bumps on a real particle would stick to each other, due to the normal force pressing them together, and elongate in the tangential direction resulting in an elastic force proportional to the elastic tangential displacement. The tangential displacement is defined to be zero at the initial time of contact, and its rate of change is given by

$$\frac{d\boldsymbol{\delta}_{ij}^t}{dt} = \mathbf{v}_{ij}^t - \frac{(\boldsymbol{\delta}_{ij}^t \cdot \mathbf{v}_{ij}) \hat{\mathbf{n}}_{ij}}{r_{ij}}, \quad (9)$$

where the first term is the relative tangential velocity at the contact point, and the second term ensures that $\boldsymbol{\delta}_{ij}^t$ remains normal to $\hat{\mathbf{n}}_{ij}$. The second term is always orthogonal to the spring direction and, hence, does not affect the rate of change of the spring length: it simply rotates it, thus keeping it tangential.

When the tangential to normal force ratio becomes larger than the particle contact friction coefficient, μ_c , for a real particle the bumps would slip against each other. Their elongation is then shortened until the bumps can stick to each other again. This is modelled by a static yield criterion, truncating the magnitude of $\boldsymbol{\delta}_{ij}^t$ as necessary to satisfy $|\mathbf{f}_{ij}^t| \leq \mu_c |\mathbf{f}_{ij}^n|$. Thus, the contact surfaces are treated as stuck while $|\mathbf{f}_{ij}^t| < \mu_c |\mathbf{f}_{ij}^n|$ and as slipping otherwise, when the yield criterion is satisfied¹.

The total force on particle i is a combination of contact forces \mathbf{f}_{ij} with other particles and external forces such as gravity \mathbf{g} . The resulting force \mathbf{f}_i and torque \mathbf{q}_i acting on particle i are

$$\mathbf{f}_i = \mathbf{g} + \sum_{j=1, j \neq i}^N \mathbf{f}_{ij}, \quad \text{and} \quad \mathbf{q}_i = \sum_{j=1, j \neq i}^N \mathbf{b}_{ij} \times \mathbf{f}_{ij}. \quad (10)$$

Finally, using these expressions we arrive at Newton's equations of motion for the translational and rotational degrees of freedom,

$$m_i \frac{d^2 \mathbf{r}_i}{dt^2} = \mathbf{f}_i, \quad \text{and} \quad I_i \frac{d}{dt} \boldsymbol{\omega}_i = \mathbf{q}_i, \quad (11)$$

with m_i the mass and I_i the inertia of particle i . We integrate (11) forward using Velocity-Verlet [AT93], formally second order in time, with an adequate time step of $\Delta t = t_c/50$. The collision time t_c is given by (5), while (9) is integrated using first-order forward Euler.

Hereafter, we distinguish between identical free flowing and identical fixed basal particles. Base particles are modelled as having an infinite mass and are unaffected by body forces: they do not move. This leaves two distinct types of collision: flow-flow, and flow-base. Model parameters for each of these collision types are set independently.

3 Statistics

3.1 Coarse-graining

The main aims of this paper are to use discrete particle simulations to both confirm the assumptions of and provide the required closure rules for the depth-averaged shallow-water

¹ Meant for review stage only. It should be noted that in the absence of dissipative forces and slipping, the system can be described as an Hamiltonian system: see Appendix A. Appendix B contains details on the tangential displacement. A pseudocode of the tangential force calculation is provided in Appendix C.

equations. Hence, continuum fields have to be extracted from the discrete particle data. There are many papers in the literature on how to go from the discrete to the continuum: binning micro-scale fields into small volumes [IK50, SH82, Lud04, Lud09, LLV⁺01], averaging along planes [TED95], or coarse graining spatially and temporally [Bab97, SA04, Gol10]. Here, we use the coarse-graining approach described by [WTLB11] as this is still valid within one course-graining width of the boundary.

The coarse-graining method has the following advantages over other methods: (i) the fields produced automatically satisfy the equations of continuum mechanics, even near the flow base; (ii) it is neither assumed that the particles are rigid nor spherical; and, (iii) the results are even valid for single particles as no averaging over groups of particles is required. The only assumptions are that each particle pair has a single point of contact (*i.e.*, the particle shapes are convex), the contact area can be replaced by a contact point (*i.e.*, the particles are not too soft), and that collisions are not instantaneous.

3.2 Mass and momentum balance

3.2.1 Notation and basic ideas

Vectorial and tensorial components are denoted by Greek letters in order to distinguish them from the Latin particle indices i, j . Bold vector notation will be used when convenient.

Assume a system given by N_f flowing particles and N_b fixed basal particles with $N = N_f + N_b$. Since we are interested in the flow, we will calculate macroscopic fields pertaining to the flowing particles only. From statistical mechanics, the microscopic mass density of the flow, ρ^{mic} , at a point \mathbf{r} at time t is defined by

$$\rho^{\text{mic}}(\mathbf{r}, t) = \sum_{i=1}^{N_f} m_i \delta(\mathbf{r} - \mathbf{r}_i(t)), \quad (12)$$

where $\delta(\mathbf{r})$ is the Dirac delta function and m_i is the mass of particle i . The following definition of the macroscopic density of the flow is used

$$\rho(\mathbf{r}, t) = \sum_{i=1}^{N_f} m_i \mathscr{W}(\mathbf{r} - \mathbf{r}_i(t)), \quad (13)$$

thus replacing the Dirac delta function in (12) by an integrable 'coarse-graining' function \mathscr{W} whose integral over space is unity. We will take the coarse-graining function to be a Gaussian

$$\mathscr{W}(\mathbf{r} - \mathbf{r}_i(t)) = \frac{1}{(\sqrt{2\pi}w)^3} \exp\left(-\frac{|\mathbf{r} - \mathbf{r}_i(t)|^2}{2w^2}\right) \quad (14)$$

with width or variance w . Other choices of the coarse-graining function are possible, but the Gaussian has the advantage that it produces smooth fields and the required integrals can be analysed exactly. According to Goldhirsch [Gol10], the coarse-graining field depends only weakly on the choice of function, and the width w is the key parameter.

It is clear that as $w \rightarrow 0$ the macroscopic density defined in (14) reduces to the one in (13). The coarse-graining function can also be seen as a convolution integral between the micro and macro definitions, i.e.,

$$\rho(\mathbf{r}, t) = \int \mathcal{W}(\mathbf{r} - \mathbf{r}') \rho^{\text{mic}}(\mathbf{r}', t) d\mathbf{r}'. \quad (15)$$

3.2.2 Mass balance

Next we will consider how to obtain the other fields of interest: the momentum density vector and the stress tensor. As stated in Sect. 3.1 the macroscopic variables will be defined in a way compatible with the continuum conservation laws.

The coarse grained momentum density vector $\mathbf{p}(\mathbf{r}, t)$ is defined by

$$p_\alpha(\mathbf{r}, t) = \sum_{i=1}^{N_f} m_i v_{i\alpha} \mathcal{W}(\mathbf{r} - \mathbf{r}_i), \quad (16)$$

where the $v_{i\alpha}$'s are the velocity components of particle i . The macroscopic velocity field $\mathbf{V}(\mathbf{r}, t)$ is then defined as the ratio of momentum and density fields,

$$V_\alpha(\mathbf{r}, t) = p_\alpha(\mathbf{r}, t) / \rho(\mathbf{r}, t). \quad (17)$$

It is straightforward to confirm that equations (13) and (16) satisfies exactly the continuity equation

$$\frac{\partial \rho}{\partial t} + \frac{\partial p_\alpha}{\partial r_\alpha} = 0, \quad (18)$$

with the Einstein summation convention for Greek letters.

3.2.3 Momentum balance

Finally, we will consider the momentum conservation equation with the aim of establishing the macroscopic stress field. In general, the desired momentum balance equations are written as,

$$\frac{\partial p_\alpha}{\partial t} = -\frac{\partial}{\partial r_\beta} [\rho V_\alpha V_\beta] + \frac{\partial \sigma_{\alpha\beta}}{\partial r_\beta} + \rho g_\alpha, \quad (19)$$

where $\sigma_{\alpha\beta}$ is the stress tensor, and g_α is the gravitational acceleration vector.

Expressions (16) and (17) for the momentum \mathbf{p} and the velocity \mathbf{V} have already been defined. The next step is to

compute their temporal and spatial derivatives, respectively, and reach closure. Taking the time derivative of (16) gives

$$\begin{aligned} \frac{\partial p_\alpha}{\partial t} &= \frac{\partial}{\partial t} \sum_{i=1}^{N_f} m_i v_{i\alpha}(t) \mathcal{W}(\mathbf{r} - \mathbf{r}_i(t)) \\ &= \sum_{i=1}^{N_f} m_i \dot{v}_{i\alpha} \mathcal{W}(\mathbf{r} - \mathbf{r}_i) + \sum_{i=1}^{N_f} m_i v_{i\alpha} \frac{\partial}{\partial t} \mathcal{W}(\mathbf{r} - \mathbf{r}_i). \end{aligned} \quad (20)$$

Using (11), the first term in (20) can be expressed as

$$A_\alpha \equiv \sum_{i=1}^{N_f} m_i \dot{v}_{i\alpha} \mathcal{W}(\mathbf{r} - \mathbf{r}_i) = \sum_{i=1}^{N_f} f_{i\alpha} \mathcal{W}(\mathbf{r} - \mathbf{r}_i). \quad (21)$$

In the simulations presented later the force on each particle contains three contributions: particle-particle interactions, particle-base interactions, and the gravitational body force. Hence,

$$f_{i\alpha} = \sum_{j=1, j \neq i}^{N_f} f_{ij\alpha} + \sum_{k=1}^{N_b} f_{ik\alpha}^b + m_i g_\alpha, \quad (22)$$

where f_{ij} is the interaction force between particle i and j , and f_{ik}^b the interaction between particle i and base particle k , or base wall if the base is flat. Therefore, we rework (21) as

$$A_\alpha = \sum_{i=1}^{N_f} \sum_{j=1, j \neq i}^{N_f} f_{ij\alpha} \mathcal{W}_i + \sum_{i=1}^{N_f} \sum_{k=1}^{N_b} f_{ik\alpha}^b \mathcal{W}_i + \sum_{i=1}^{N_f} m_i \mathcal{W}_i g_\alpha, \quad (23)$$

where $\mathcal{W}_i = \mathcal{W}(\mathbf{r} - \mathbf{r}_i)$. The last term in (23) can be simplified to ρg_α by using (13). From Newton's third law, the contact forces are equal and opposite, such that $f_{ij} = -f_{ji}$. Hence,

$$\sum_{i=1}^{N_f} \sum_{j=1, j \neq i}^{N_f} f_{ij\alpha} \mathcal{W}_i = \sum_{i=1}^{N_f} \sum_{j=1, i \neq j}^{N_f} f_{ji\alpha} \mathcal{W}_j = -\sum_{i=1}^{N_f} \sum_{j=1, i \neq j}^{N_f} f_{ij\alpha} \mathcal{W}_j, \quad (24)$$

where in the first step we interchanged the dummy summation indices. It follows from (24) that (23) can be written as

$$\begin{aligned} A_\alpha &= \frac{1}{2} \sum_{i=1}^{N_f} \sum_{j=1, j \neq i}^{N_f} f_{ij\alpha} (\mathcal{W}_i - \mathcal{W}_j) + \sum_{i=1}^{N_f} \sum_{k=1}^{N_b} f_{ik\alpha}^b \mathcal{W}_i + \rho g_\alpha \\ &= \sum_{i=1}^{N_f} \sum_{j=i+1}^{N_f} f_{ij\alpha} (\mathcal{W}_i - \mathcal{W}_j) + \sum_{i=1}^{N_f} \sum_{k=1}^{N_b} f_{ik\alpha}^b \mathcal{W}_i + \rho g_\alpha. \end{aligned} \quad (25)$$

Next, we will write A_α as the divergence of a tensor in order to obtain a formula for the stress tensor. The following identity holds for any smooth function \mathcal{W}

$$\begin{aligned} \mathcal{W}_j - \mathcal{W}_i &= \int_0^1 \frac{\partial}{\partial s} \mathcal{W}(\mathbf{r} - \mathbf{r}_i + s\mathbf{r}_{ij}) ds \\ &= r_{ij\beta} \frac{\partial}{\partial r_\beta} \int_0^1 \mathcal{W}(\mathbf{r} - \mathbf{r}_i + s\mathbf{r}_{ij}) ds, \end{aligned} \quad (26)$$

where $\mathbf{r}_{ij} = \mathbf{r}_i - \mathbf{r}_j$; we used the chain rule and differentiation to the full argument of $\mathcal{W}(\cdot)$ per component.

The next step extends the coarse-graining method to account for boundary forces. To obtain a similar expression for the interaction with base particles, we write

$$\begin{aligned} -\mathcal{W}_i &= \int_0^\infty \frac{\partial}{\partial s} \mathcal{W}(\mathbf{r} - \mathbf{r}_i + s\mathbf{r}_{ik}) ds \\ &= r_{ik\beta} \frac{\partial}{\partial r_\beta} \int_0^\infty \mathcal{W}(\mathbf{r} - \mathbf{r}_i + s\mathbf{r}_{ik}) ds, \end{aligned} \quad (27)$$

which holds because \mathcal{W}_i decays towards infinity. Substituting identities (26), (27) and (13) into (25) leads to

$$\begin{aligned} A_\alpha &= -\frac{\partial}{\partial r_\beta} \sum_{i=1}^{N_f} \sum_{j=i+1}^{N_f} f_{ij\alpha} r_{ij\beta} \int_0^1 \mathcal{W}(\mathbf{r} - \mathbf{r}_i + s\mathbf{r}_{ij}) ds \\ &\quad - \frac{\partial}{\partial r_\beta} \sum_{i=1}^{N_f} \sum_{k=1}^{N_b} f_{ik\alpha}^b r_{ik\beta} \int_0^\infty \mathcal{W}(\mathbf{r} - \mathbf{r}_i + s\mathbf{r}_{ik}) ds + \rho g_\alpha. \end{aligned} \quad (28)$$

From [Gol10], it follows that the second term in (20) can be expressed as follows

$$\sum_i^{N_f} m_i v_{i\alpha} \frac{\partial}{\partial t} \mathcal{W}(\mathbf{r} - \mathbf{r}_i) = -\frac{\partial}{\partial r_\beta} \left[\rho V_\alpha V_\beta + \sum_i^{N_f} m_i v'_{i\alpha} v'_{i\beta} \mathcal{W}_i \right], \quad (29)$$

where v'_i is the fluctuating velocity of particle i , with components given by

$$v'_{i\alpha}(t, \mathbf{r}) = v_{i\alpha}(t) - V_\alpha(\mathbf{r}, t). \quad (30)$$

Substituting (28) and (29) into momentum balance (19) yields

$$\begin{aligned} \frac{\partial \sigma_{\alpha\beta}}{\partial r_\beta} &= \frac{\partial}{\partial r_\beta} \left[-\sum_{i=1}^{N_f} \sum_{j=i+1}^{N_f} f_{ij\alpha} r_{ij\beta} \int_0^1 \mathcal{W}(\mathbf{r} - \mathbf{r}_i + s\mathbf{r}_{ij}) ds \right. \\ &\quad \left. - \sum_{i=1}^{N_f} \sum_{k=1}^{N_b} f_{ik\alpha}^b r_{ik\beta} \int_0^\infty \mathcal{W}(\mathbf{r} - \mathbf{r}_i + s\mathbf{r}_{ij}) ds - \sum_i^{N_f} m_i v'_{i\alpha} v'_{i\beta} \mathcal{W}_i \right]. \end{aligned} \quad (31)$$

Therefore the stress is given by

$$\begin{aligned} \sigma_{\alpha\beta} &= -\sum_{i=1}^{N_f} \sum_{j=i+1}^{N_f} f_{ij\alpha} r_{ij\beta} \int_0^1 \mathcal{W}(\mathbf{r} - \mathbf{r}_i + s\mathbf{r}_{ij}) ds \\ &\quad - \sum_{i=1}^{N_f} \sum_{k=1}^{N_b} f_{ik\alpha}^b r_{ik\beta} \int_0^\infty \mathcal{W}(\mathbf{r} - \mathbf{r}_i + s\mathbf{r}_{ik}) ds - \sum_i^{N_f} m_i v'_{i\alpha} v'_{i\beta} \mathcal{W}_i. \end{aligned} \quad (32)$$

In our simulations the tangential forces contribute less than 6% to the total stress in the system, such that the stress is almost symmetric.

Equation (32) differs from the results of [Gol10] by an additional term that accounts for the stress created by the

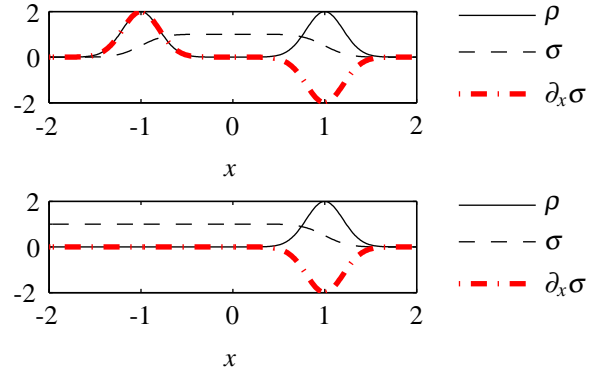


Fig. 1: Stress and density profiles are shown for two one-dimensional two-particle systems, each with two particles of unit mass at positions $x = \pm 1$, and repelling each other (so with $d > 2$ for our granular case). In the top figure, both particles are flowing, while in the bottom figure the left particle is fixed and the right one flowing.

presence of the base, as detailed in [WTLB11]. The contribution to the stress from the interaction of two flow particles i, j is spatially distributed along the contact line from \mathbf{r}_i to \mathbf{r}_j , while the contribution from the interaction of particles i with a fixed particle k is distributed along the line from \mathbf{r}_i to \mathbf{r}_k , extending further beyond \mathbf{r}_k . We explain the situation as follows, see Fig. 1. Stress and density profiles are calculated using (15) and (32) for two one-dimensional two-particle systems, each with two particles of unit mass at positions $x = \pm 1$, repelling each other with a force $|f| = 1$ and with $w = 0.2$. In the top figure, both particles belong to the flowing species, so the density is distributed around the particles' centre of mass and the stress along the contact line. In the bottom figure, the left particle is a fixed base particle and the right particle is a free flowing one, so density is distributed around the flowing particle's centre of mass and the stress along the line extending from the flowing particle to negative infinity.

The strength of this method is that the spatial coarse graining fields by construction satisfy the mass and momentum balance equations exactly at any given time, irrespective of the choice of the coarse graining function. Further details about the accuracy of the stress definition (32) are discussed in [WTLB11]. The expression for the energy is also not treated in this publication, we refer the interested reader to [Bab97].

4 Mathematical background

In this section, we briefly outline the existing knowledge on continuum shallow-layer theories for granular flow.

4.1 Shallow-layer model

Shallow-layer granular models have been shown to be an effective tool in modelling many geophysical mass flows. Early granular models were formulated by adding gravitational acceleration and Coulomb basal friction to shallow-layer fluid models [GEY67, KE73]. Similar dry granular models have been derived using the long-wave approximation [SH89, HSSN93, Ive97, GWH99, WGH99] for shallow variations in the flow height and slope topography and included a Mohr-Coulomb rheology via the use of an earth pressure coefficient. The key to these theories is to depth-integrate general three-dimensional equations in the shallow direction, resulting in a system of two-dimensional equations which still retains some information about variations in thickness.

Let $Oxyz$ be a coordinate system with the x -axis down-slope and the z -axis normal to a channel with mean slope θ . For simplicity, we further consider boundaries, flows, and external forcing to be (statistically) uniform in y . The continuum macro-scale fields are thus independent of y , while the DPM simulations remain three-dimensional and will be periodic in y . The free-surface and base location are $z = s(x, t)$ and $z = b(x)$, respectively. The thickness of the flow is thus $h(x, t) = s(x, t) - b(x)$, and the bulk density and velocity components are ρ and $\mathbf{u} = (u, v = 0, w)^t$, respectively, as functions of x, y, z and t .

The three-dimensional flow viewed as continuum is described by the mass and momentum balance equations (18) and (19). At the top and bottom surface, kinetic boundary conditions are satisfied: $D(z - s)/Dt = 0$ and $D(z - b)/Dt = 0$ at their respective surfaces, and with material time derivative

$$D(\cdot)/Dt = \partial(\cdot)/\partial t + u\partial(\cdot)/\partial x + w\partial(\cdot)/\partial z$$

(since we assumed $v = 0$). Furthermore, the top surface is traction-free, while the traction at the basal surface is essentially Coulomb-like. We decompose the traction $\mathbf{t} = \mathbf{t}_t + t_n \hat{\mathbf{n}}$ in tangential and normal components, with normal component of the traction $t_n = -\hat{\mathbf{n}} \cdot (\boldsymbol{\sigma} \hat{\mathbf{n}})$, where $\hat{\mathbf{n}}$ is the outward normal at the fixed base and $\boldsymbol{\sigma}$ is the stress tensor. The Coulomb ansatz implies that $\mathbf{t}_t = -\mu |\mathbf{t}_n| \mathbf{u} / |\mathbf{u}|$ with friction factor $\mu > 0$. Note that μ generally can be a function of the local thickness and the flow velocity. Its determination is essential to find a closed system of shallow-layer equations.

We consider flows that are shallow, such that a typical aspect ratio ε between flow thickness and length, normal and alongslope velocity, or normal and downslope variations in basal topography, is small, of order $\mathcal{O}(\varepsilon)$. Furthermore, the typical friction factor μ is small enough to satisfy $\mu = \mathcal{O}(\varepsilon^\gamma)$ with $\gamma \in (0, 1)$. We follow the derivation of the depth-averaged shallow layer equations for granular flow presented in [BT12] without assuming that the flow is incompressible. Instead we start the asymptotic analysis from

the dimensionless form of the mass and momentum conservation equations (18) and (19), assuming only that the density is independent of depth at leading order. Density, velocity, and stress are depth averaged as follows

$$\bar{(\cdot)} = \frac{1}{h} \int_b^s (\cdot) dz. \quad (33)$$

In the end, we retain the normal stress ratio $K = \bar{\sigma}_{xx} / \bar{\sigma}_{zz}$, the shape factor $\alpha = \overline{u^2} / \bar{u}^2$, and the friction μ as unknowns. The goal is to investigate whether these unknowns can be expressed as either constants or functions of the remaining shallow flow variables, to leading order in $\mathcal{O}(\varepsilon)$. The latter variables are the flow thickness $h = h(x, t)$ and the depth-averaged velocity $\bar{u} = \bar{u}(x, t)$. At leading order, the momentum equation normal to the base yields that the downward normal stress is lithostatic, $\bar{\sigma}_{zz}(z) = \bar{\rho} g \cos \theta (s - z) + \mathcal{O}(\varepsilon)$. Depth-averaging the remaining equations, while retaining only terms of order $\mathcal{O}(\varepsilon^{1+\gamma})$, yields the dimensional depth-averaged shallow-layer equations, cf. [VATK⁺07, BT12],

$$\frac{\partial(\bar{\rho}h)}{\partial t^*} + \frac{\partial}{\partial x^*} (\bar{\rho}h\bar{u}) = 0, \quad (34a)$$

$$\frac{\partial}{\partial t^*} (h\bar{\rho}\bar{u}) + \frac{\partial}{\partial x^*} \left(h\bar{\rho}\alpha\bar{u}^2 + \frac{K}{2}gh^2\bar{\rho}\cos\theta \right) = gh\bar{\rho}S, \quad (34b)$$

with

$$S = \sin\theta - \mu \frac{\bar{u}}{|\bar{u}|} \cos\theta - \frac{\partial b}{\partial x^*} \cos\theta. \quad (34c)$$

To demarcate the dimensional time and spatial scales, we have used starred coordinates. These scales differ from the ones used before in the particle dynamics and the dimensionless ones used later in the DPM simulations. The shallow-layer equations (34) consist of the continuity equation (34a) and the downslope momentum equation (34b). The system arises also via a straightforward control volume analysis of a column of granular material viewed as continuum from base to the free surface, using Reynolds-stress averaging and a leading order closure with depth averages.

While the mean density $\bar{\rho}$ can be modelled as a system variable by considering the energy balance equation, we will assume that it can be expressed as a function of height and velocity $\bar{\rho}(h, \bar{u})$. Thus, the closure to equations (34) is determined when we can find the functions $\bar{\rho}(h, \bar{u})$, $K(h, \bar{u})$, $\alpha(h, \bar{u})$, and $\mu(h, \bar{u})$. In Section 9.2, we will analyse if and when DPM simulations can determine these functions.

4.2 Granular friction laws for a rough basal surface

The friction coefficient, μ , was originally [SH89] taken to be a simple Coulomb type $\mu = \tan \delta$, where δ is a fixed friction angle. Note that in steady state for a flat base with $b = 0$, the shallow-layer momentum equation (34b) then yields

$\mu = \tan \theta$. Pure Coulomb friction implies that there is only one inclination, $\theta = \delta$, at which steady flow of constant height and flow velocity exists. That turns out to be unrealistic. Three parameterisations for μ have been proposed in the literature.

Firstly, Forterre and Pouliquen [FP03] found steady flow in laboratory investigations for a range of inclinations concerning flow over rough basal surfaces. They measured the thickness h_{stop} of stationary material, left behind when a flowing layer was brought to rest, with the following fit

$$\frac{h_{stop}(\theta)}{Ad} = \frac{\tan(\delta_2) - \tan(\theta)}{\tan(\theta) - \tan(\delta_1)}, \quad \delta_1 < \theta < \delta_2, \quad (35)$$

where δ_1 is the minimum angle required for flow, δ_2 the maximum angle at which steady uniform flow is possible, d the particle diameter, and A a characteristic dimensionless length scale over which the friction varies. Note that h_{stop} diverges for $\theta = \delta_1$ and is zero for $\theta = \delta_2$. For $h > h_{stop}$, steady flow exists in which the Froude number, the aspect ratio between flow speed and surface gravity-wave speed ($F = \bar{u}/\sqrt{g \cos \theta h}$), is a linear function of the height,

$$F = \beta \frac{h}{h_{stop}(\theta)} - \gamma, \quad \text{for } \delta_1 < \theta < \delta_2, \quad (36)$$

where β and γ are constants independent of chute inclination and particle size. Provided one assumes the steady state $\mu = \tan \theta$ to hold (approximately) in the dynamic case as well, it can be combined with (35) and (36) to find an improved empirical friction law

$$\mu = \mu^*(h, F) = \tan(\delta_1) + \frac{\tan(\delta_2) - \tan(\delta_1)}{\beta h / (Ad(F + \gamma)) + 1}. \quad (37)$$

This is a closure for μ in terms of the flow variables, and has been shown to have practical value. Note, that in the limit $\delta_1 \rightarrow \delta_2 = \delta$ the Coulomb model is recovered.

Secondly, in an earlier version [Pou99], another, exponential fitting was proposed for h_{stop} , as follows

$$\frac{h'_{stop}(\theta)}{A'd} = \ln \frac{\tan(\theta) - \tan(\delta'_1)}{\tan(\delta'_2) - \tan(\delta'_1)}, \quad \text{for } \delta'_1 < \theta < \delta'_2 \quad (38)$$

with the same limiting behaviour, and primes used to denote the difference in the fit. It yields the friction factor

$$\mu = \mu'(h, F) = \tan \delta'_1 + (\tan \delta'_2 - \tan \delta'_1) e^{\left\{ \frac{-\beta' h}{A'd(F + \gamma')} \right\}}. \quad (39)$$

Equation (35) did, however, prove to be a better fit to experiments and is computationally cheaper to evaluate.

Finally, [Jen06] included a modified dissipation in the kinetic theory equations and was able to produce a law very similar to the original experimentally obtained model (36), *i.e.*

$$F = \beta_J \frac{h}{h_{stop}(\theta)} \frac{\tan^2(\theta)}{\tan^2(\delta_1)} - \gamma_J, \quad (40)$$

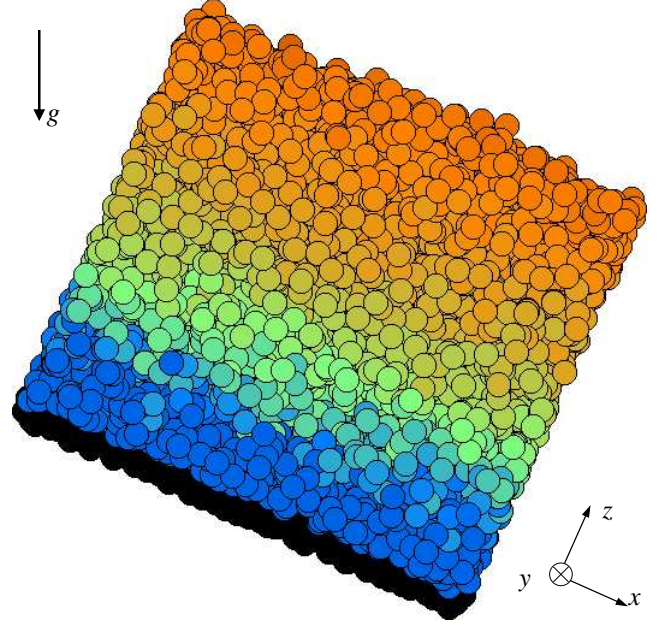


Fig. 2: DPM simulation for $N_f/200 = 17.5$, inclination $\theta = 24^\circ$ and the diameter ratio of free and fixed particles, $\lambda = 1$, at time $t = 2000$; gravity direction g as indicated. The domain is periodic in x - and y -directions. In the z -direction, fixed particles (black) form a rough base while the surface is unconstrained. Colours indicate speed: increasing from blue via green to orange.

for which we can use any appropriate fit for h_{stop} . It leads subsequently to a more complicated evaluation of the friction law for μ . We omit further details and compare our DPM simulations against these rules, using fits for the rough basal surface. Additionally, we use the DPM to investigate how to extend these laws to smoother surfaces.

5 Simulation description

In this section, DPM is used to simulate monodispersed granular flows.

Parameters have been nondimensionalised such that the flow particle diameter $d = 1$, mass $m = 1$ and the magnitude of gravity $g = 1$. The normal spring and damping constants are $k^n = 2 \cdot 10^5 mg/d$ and $\gamma^n = 50 \sqrt{g/d}$; thus the contact duration is $t_c = 0.005 \sqrt{d/g}$ and the coefficient of restitution is $\varepsilon = 0.88$. The tangential spring and damping constants are $k^t = (2/7)k^n$ and $\gamma^t = \gamma^n$, such that the frequency of normal and tangential contact oscillation and the normal and tangential dissipation are equal. The microscopic friction coefficient was taken to be $\mu^c = 1/2$.

The interaction parameters are chosen as in Silbert *et al.* [SEG⁺01] to simulate glass particles of 0.1 mm size; this corresponds to a dimensional time scale of $\sqrt{d/g} = 3.1$ ms

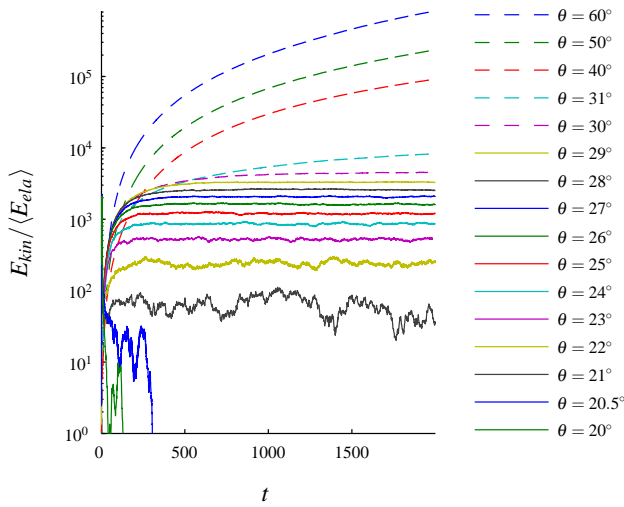


Fig. 3: The ratio of kinetic to mean elastic energy plotted against time for $N_f/200 = 20$ flowing particles, basal roughness $\lambda = 1$, and varying chute angles θ . Flow stops for inclinations $\theta \leq 20.5^\circ$, remains steady for $21^\circ \leq \theta \leq 29^\circ$ and accelerates for $\theta \geq 30^\circ$ (dashed lines).

and dimensional velocity scale $\sqrt{dg} = 0.031 \text{ ms}^{-1}$. The above parameters are identical to the simulations of Silbert *et al.*, except that dissipation in tangential direction, γ^t , was added to damp rotational degrees of freedom in arresting flow. Adding of such tangential damping removes all vibrational energy for flows otherwise arrested. Silbert *et al.* also investigated the sensitivity of the results to the particle interaction parameters t_c , ε , the ratio k^n/k^t , and μ^c ; they found that while the density of the bulk material is not sensitive to these interaction parameters, the flow velocity increased with decreasing friction μ^c . Nonetheless, the qualitative behaviour of the velocity profiles did not change.

The chute is periodic and of size 20×10 in the x - and y -directions and has a layer of fixed particles as a base. The bottom particles are monodispersed with (nondimensional) diameter λd . Various basal roughnesses are investigated by taking $\lambda = 0$ to 4 in turn, with $\lambda = 0$ as flat base. This bottom particle layer is obtained by performing a simulation on a horizontal, smooth-bottom chute. It is filled with a randomly distributed set of particles of diameter λd and we simulate until a static layer about 12 particles thick is produced. Then a slice of particles with centres between $z \in [9.3, 11]\lambda d$ are fixed and translated 11 diameters downwards to form the base. The layer is thick enough to ensure that no flowing particles can fall through the rough base during the full simulations. Their positions are fixed.

Initially, N_f particles are inserted into the chute. To insert a particle, a random location $(x, y, z) \in [0, 20] \times [0, 10] \times [0, H]$ is chosen, where $H = N_f/200$ initially. If the particle at this position overlaps other particles, the insertion is re-

jected, and the insertion domain is enlarged by increasing H to $H + 0.01$ to ensure that there is enough space for all particles. This process creates an initial packing fraction of about $\rho/\rho_p = 0.3$. Once the simulation starts the particles initially compact to an approximated height $N_f/200$, giving the particles in the chute enough kinetic energy to initialise flow. Dimensionless time is integrated between $t \in [0, 2000]$ to allow the system to reach a steady state. A screenshot of the system in steady state is given in Fig. 2.

To ensure that the size of the periodic box does not influence the result, we compared density and velocity profiles of the flow at an angle $\theta = 24^\circ$ and $N_f/200 = 17.5$ for domain sizes $L_x = 10, 20, 40$, $L_y = 10$ and $L_x = 10, 20, 40$, $L_y = L_x/2$, and saw no significant changes.

6 Arrested, steady, and accelerating flow

From the experiments of Pouliquen [Pou99], granular flow over a rough base is known to exist for a range of heights and inclinations. DPMs by [SEG⁺01] also showed that steady flows arose for a range of flow heights and (depth-averaged) velocities or Froude numbers. Their simulations did, however, provide relatively few data points near the boundary of arrested and steady flow to allow a more adequate fit of the stopping height. The original data of Silbert *et al.* is indicated by the red crosses in Fig. 4. In this section, we therefore perform numerous DPMs at heights and angles near the demarcation line between the steady flow regime and the regime with static piles. To study the full range of steady flow regimes, simulations were performed for inclinations θ varying between 20° and 60° and $N_f/200 = 10, 20, 30$, and 40. In Section 8, we will repeat (some of) these simulations for varying base roughness.

We define the flow as steady if the ratio of kinetic energy normalised by the mean elastic potential energy becomes time independent. This is shown in Fig. 3, where we plot such an energy ratio for a rough base, constant height, and varying chute angle. The elastic potential energy is averaged over $t \in [1000, 2000]$ to minimise fluctuations after start-up, but any interval larger than 100 appears sufficient. For chute angles at most 20.5° the kinetic energy vanishes after a short time, thus the flow arrests; for chute angles between $21^\circ - 29^\circ$, a constant value is reached, indicating steady flow; and, for inclinations above 29° the energy keeps increasing: thus flow steadily accelerates. If the energy ratio remained constant within $t \in [1800, 2000]$, the flow was deemed steady, otherwise the flow was deemed to be either accelerating or stopping.

Unlike fluids, the free surface of granular flows, and thus the flow height, are not well defined. In [SEG⁺01], the height of the flow was estimated by $N_f/200$, which is equivalent to assuming a constant packing fraction of $\rho/\rho_p = \pi/6$. However, the exact height $h = s - b$ of the flow varies from

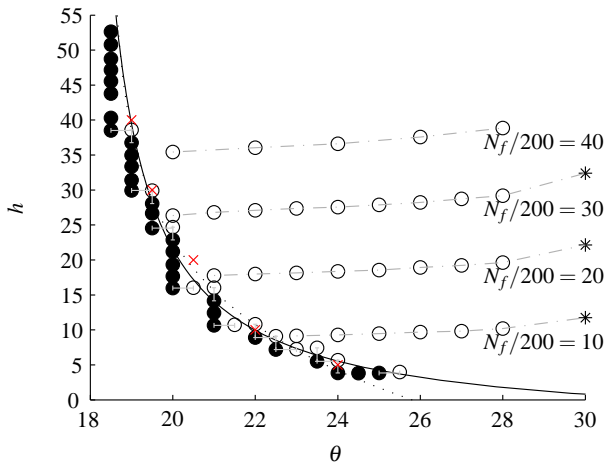


Fig. 4: Overview of DPM results for $\lambda = 1$, with markers denoting the flow state at $t = 2000$: arrested \bullet , steady \circ , and accelerating $*$ flows. Grey dash-dotted lines mark thickness h for fixed $N_f/200 = 10, 20, 30$, and 40 . The demarcation line is fitted to $h_{stop}(\theta)$ in equation (35) (solid line) and $h'_{stop}(\theta)$ in (38) (dotted line). Error bars mark intervals establishing the demarcation line. Red crosses denote the demarcation between arrested and accelerating flow found in [SEG⁺01].

the approximated height due to compaction of the flow and $N_f/200$ is typically an overestimate. In [VATK⁺07], the surface of the flow was defined by the time-average of the maximum vertical position of all flow particles. One could also define the free surface of the flow as the height where the density vanishes. The latter two methods, however, have the disadvantage that saltating particles can lead to slightly overestimated flow heights.

Instead, we will define the height via the downward normal stress. For steady uniform flows the downward normal stress is lithostatic, *i.e.*, balances the gravitational weight, such that

$$\sigma_{zz}(z) = \int_z^\infty \rho(z') g \cos \theta dz'. \quad (41)$$

This is a direct consequence of the momentum balance equations. Thus, $\sigma_{zz}(z)$ has to decrease monotonically; the base and free surface are the heights at which $\sigma_{zz}(z)$ reaches its maximum and minimum value, respectively. However, in order to avoid effects of coarse graining or single particles near the boundary, we cut off the stress $\sigma_{zz}(z)$ on either boundary by defining threshold heights

$$z_1 = \min\{z : \sigma_{zz} < (1 - \kappa) \max_{z \in \mathbb{R}} \sigma_{zz}\} \quad \text{and} \quad (42a)$$

$$z_2 = \max\{z : \sigma_{zz} > \kappa \max_{z \in \mathbb{R}} \sigma_{zz}\} \quad (42b)$$

with $\kappa = 2\%$. We subsequently linearly extrapolate the stress profile in the interval (z_1, z_2) to define the base b and surface height s as the height at which the linear extrapolation

reaches the maximum and minimum values of σ_{zz} , respectively,

$$b = z_1 - \frac{\kappa}{1 - 2\kappa}(z_2 - z_1), \quad s = z_2 + \frac{\kappa}{1 - 2\kappa}(z_2 - z_1). \quad (42c)$$

The variable most sensitive to these height choices is $\bar{\rho}$. However, it shows well-defined functional behaviour for our definition of height, shown later. This is not the case if we define height by the density or the method in [VATK⁺07]. The threshold $\kappa = 2\%$ was chosen because the results in Fig. 13 were relatively insensitive to the choice of κ at or above 2%.

To determine the demarcation line $h_s(\theta; \lambda)$ between arrested and steady flow with good accuracy, we performed a set of simulations with initial conditions determined by the following algorithm. Starting from an initial ‘filling height’ $N_f/200 = 40$ and inclination $\theta = 24^\circ$, the angle was increased in steps of 1° until eventually a flowing state was reached. Then the angle was decreased by $1/2^\circ$. When the flow arrested, the number of particles was increased by 400, otherwise the angle was further decreased by $1/2^\circ$, and so forth, till $N_f/200 = 60$. Flow was defined to be arrested when the energy ratio $E_{kin}/\langle E_{ela} \rangle$ fell below 10^{-5} within 500 time units, otherwise the flow was classified as flowing. To validate this approach a few arrested flows were continued after $t = 500$, and a further decrease of kinetic energy was observed. This procedure yields intervals of the inclination angle for each height and, vice versa, height intervals for each angle, between which the demarcation line lies. The values presented in [SEG⁺01] deviate at most 0.5° from our observations, perhaps due to the preparation of the chute bottom, or the slightly different dissipation used. A demarcating curve between steady and arrested flow was fitted to equations (35) and (38) by minimising the horizontal, respectively vertical, distance of the fit to these intervals, see Fig. 4. Fitting $h_{stop}(\theta)$ yields better results than $h'_{stop}(\theta)$ for all roughnesses and only the fit (35) will be used hereafter. Similar fits will be made in Section 8 for varying basal roughness.

7 Statistics for uniform steady flow

To obtain detailed information about steady flows, we use the statistics defined in Sect. 3. Since the flows of interest are steady and uniform in x and y , density, velocity and stress will be averaged over x , y and t . The resulting depth profiles will depend strongly on the coarse-graining width w , which needs to be carefully selected. Representative depth profiles for particular heights, inclinations and basal roughnesses will also be analysed.

Depth profiles for steady uniform flow are averaged using a coarse graining width w over $x \in (0, 20]$, $y \in (0, 10]$

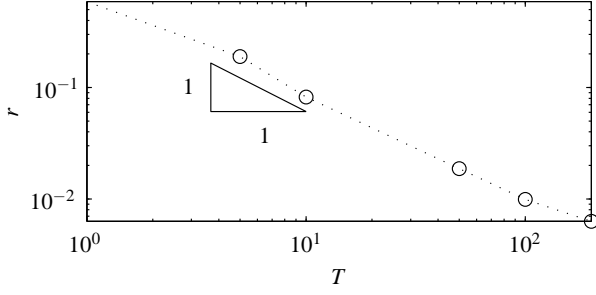


Fig. 5: Depth-averaged norm of the momentum rate of change, $r = \int_b^s |\partial_t(\rho\mathbf{u})| dz$, with $\partial_t(\rho\mathbf{u})$ determined by (44) for varying time averaging interval T . Steady flow at height $N_f/200 = 20$ and inclination $\theta = 24^\circ$ was used. Temporal fluctuations decrease inversely proportional to the length of the time averaging interval. Dotted line is for illustration only.

and $t \in [2000, 2000 + T]$. The profile of a variable χ is thus defined as

$$\langle \chi \rangle_w^T(z) = \frac{1}{200T} \int_{2000}^{2000+T} \int_0^{10} \int_0^{20} \chi_w(t, x, y, z) dx dy dt, \quad (43)$$

with χ_w in turn the macroscopic field(s) of density, momentum and stress, as defined in (13), (16) and (32). We average in time with time snapshots taken every $t_c/2$ units.

To determine an appropriate time averaging interval T , we calculate the rate of change in momentum from the density, velocity and stress fields by

$$\frac{\partial(\rho\mathbf{u})}{\partial t} = \nabla \cdot \boldsymbol{\sigma} - \rho\mathbf{g} - \mathbf{u} \cdot \nabla(\rho\mathbf{u}). \quad (44)$$

For steady flow, the temporal variations in mass and momentum should approach zero when averaged over a long enough time interval T . This is shown in Fig. 5, where we plot the depth-averaged norm of the momentum rate of change for varying time averaging interval. For $T \geq 100$, the temporal fluctuations decrease to less than 2% of the largest term, $\bar{\rho}g$, in the momentum equation. In the remainder, we choose $T = 100$ as the averaging interval.

The effect of varying coarse-graining width w is shown in Fig. 6, which shows the z -profile of particle volume fraction ρ/ρ_p , where ρ_p is the particle density. For small w we observe strong oscillations of about 0.9 particle diameters width, particularly at the base. The microscopic oscillations are increasingly smoothed out and finally vanish as we approach $w = 0.5$. For larger w , such as $w \geq 1$, the macroscopic gradients at the base and surface are smoothed out, an unwanted effect of the coarse-graining. The same behaviour is observed in the stress and velocity fields. Smoothing over the microscopic structure makes it impossible to observe microscopic layering in the density, which we still wish to

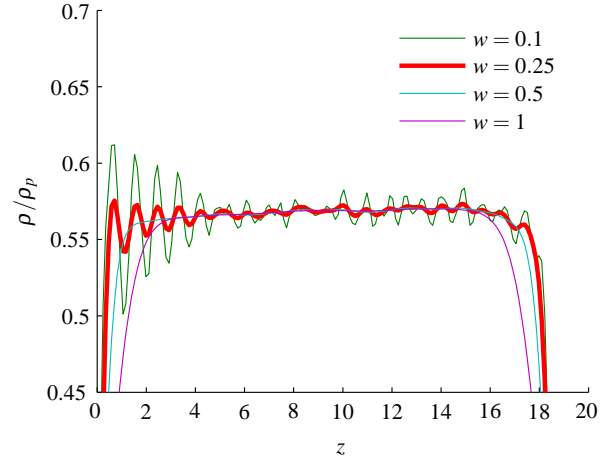


Fig. 6: Particle volume fraction ρ/ρ_p for $N_f/200 = 40$, $\theta = 24^\circ$, and $\lambda = 1$ for varying coarse graining widths w . While the density is approximately constant in the bulk, microscopic layering effects are visible for $w < 0.5$.

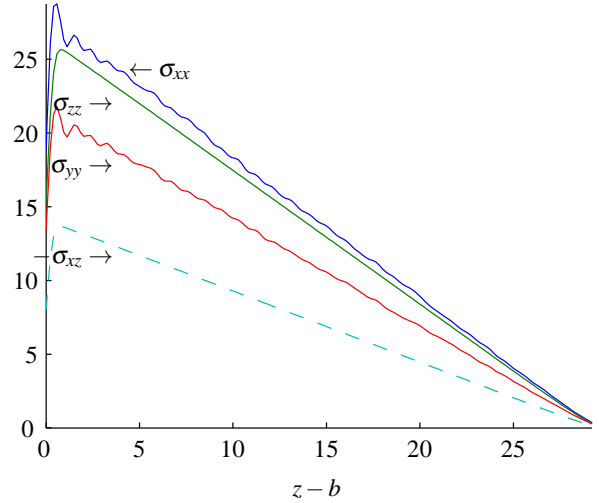


Fig. 7: Normal and shear stresses for $N_f/200 = 30$, $\theta = 28^\circ$, and roughness $\lambda = 1$. Shear σ_{xz} and downward normal stress σ_{zz} are balanced by gravitational forces. The normal stresses show anisotropic behaviour.

identify in our averaged fields. Hence, we choose $w = 0.25$ as the coarse-graining width, such that layering effects remain visible along with the rather sharp macroscopic gradients.

The microscopic oscillations at the base indicate a strong layering effect of particles near the boundary, despite the rough bottom surface. The macroscopic density throughout the flow is almost constant in the bulk and decreases slightly towards the base. An approximately constant density profile is a feature of all steady flows and is a key assumption of depth-averaging.

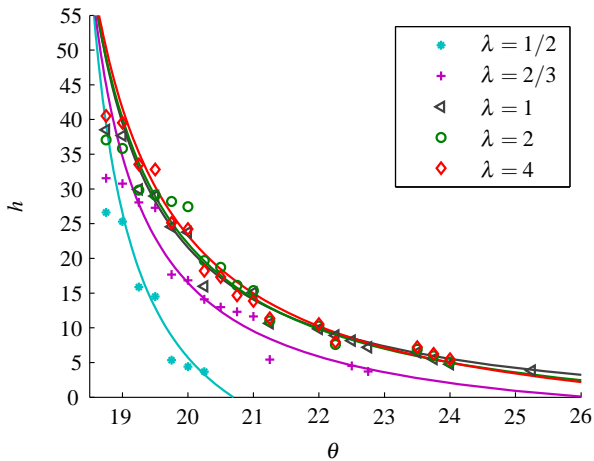


Fig. 8: Demarcation line $h_{stop}(\theta; \lambda)$ for varying basal roughness. Markers denote the midpoint of the intervals around which the curve was fitted. Steady flow is observed at smaller inclinations for smoother bases. While the smaller angle $\delta_{1,\lambda}$ varies only slightly, the larger angle $\delta_{2,\lambda}$ decreases rapidly with the smoothness. For $\lambda = 0$, the demarcation line is vertical at $\theta = 12.5^\circ$ (not shown).

Non-negligible stress components are plotted in Fig. 7. We have observed (not shown) that the stress components are nearly symmetric (the asymmetric part contributes less than 0.1% to the deviatoric stress). Shear stresses σ_{yx} and σ_{yz} are negligible since the flow velocity in y -direction vanishes. For steady flow, the downward normal stress $\sigma_{zz}(z)$ is lithostatic and satisfies equation (41) with a maximum error of 0.4%. Since the density is nearly constant, we obtain a linear stress profile, another assumption of depth-averaged theory. Applying the momentum balance (19) to steady uniform flow further yields that the shear stress satisfies $\sigma_{xz} = \int_z^\infty \rho(z') g \sin \theta dz'$. Thus, the macro-scale friction μ satisfies $\mu = \sigma_{xz} / \sigma_{zz} = -g_x / g_z = \tan \theta$. This relation is locally satisfied for all steady flow cases to an accuracy of $|\theta - \tan^{-1}(\mu)| < 0.6^\circ$. The remaining normal stress components, σ_{xx} and σ_{yy} , are not constrained by this mass balance. We thus see in Fig. 7 significant anisotropy in the amplitude of the normal stresses, in particular in σ_{yy} . The confining stress is largest in the flow direction, except for very small inclinations. It is always weakest in the lateral or y -direction with fluctuations at the base that are in phase with the fluctuations of the density. Generally, the anisotropy increases with higher inclinations and smoother bases; this will be analysed further in future work.

8 Transition from rough to smooth base

Next, we study the effect of smoother bases on the range of steady flows by decreasing the diameter λd of the base par-

ticles, with the limiting case of a flat bottom wall for $\lambda = 0$. Such an extensive numerical study of the effects of changing bottom roughness appears to be novel. To that effect, the DPM simulations from Section 6 were extended such that results for basal roughnesses $\lambda = 0, 1/2, 2/3, 5/6, 1, 1.5, 2$ and 4 can be compared. For $\lambda = 1/6$ and $\lambda = 1/3$ only simulations to calculate h_{stop} were undertaken.

A family of demarcation curves $h_{stop}(\theta; \lambda)$ between steady and arrested flow is shown in Fig. 8. The curve fits are based on

$$h_{stop}(\theta; \lambda) = A_\lambda d \frac{\tan(\delta_{2,\lambda}) - \tan(\theta)}{\tan(\theta) - \tan(\delta_{1,\lambda})}, \quad \delta_{1,\lambda} < \theta < \delta_{2,\lambda}, \quad (45)$$

in which the dependencies on λ are explicitly denoted. The fitting parameters $\delta_{1,\lambda}$, $\delta_{2,\lambda}$, A_λ appearing in (45) are given in Table 1. As in Sect. 6, a fit based on the original equation (35) (or (45)) rather than Pouliquen's early fit (38) yields the best results.

For a flat or nearly flat bottom, such that $\lambda \leq 1/6$, steady flow initiates and resides at or very tightly around one inclination for all heights, see Table 1. This is in agreement with the angle found in the laboratory experiments of [GTDD03]. For $1/3 < \lambda \leq 4$, we observe Pouliquen-style behaviour; this is shown in Fig. 8. The angle $\delta_{1,\lambda}$ of flow initiation is nearly constant with respect to λ . In contrast, the range of angles at which both steady and arrested flow is possible, $\delta_{2,\lambda} - \delta_{1,\lambda}$, is maximal for $1 \leq \lambda \leq 1.5$ and decreases for smoother chutes with $\lambda < 1$, as shown in Table 1. This has been reported for laboratory experiments in [GTDD03], who also observed a slight decrease of the interval $\delta_{2,\lambda} - \delta_{1,\lambda}$ for $\lambda > \lambda_c \approx 2$. However, their λ_c was measured for basal particles fixed at the same height and depended on the compactness of the base. We observe a slight decrease of $\delta_{2,\lambda}$ for $\lambda \geq 1.5$; however, the fitting curves in Fig. 8 do mildly overlap for $\lambda \geq 1$.

We recall that $\delta_{1,\lambda}$ and $\delta_{2,\lambda}$ are fitting parameters for the h_{stop} -curve (45) which does not necessarily imply, though it is expected, that the flow accelerates for angles greater than $\delta_{2,\lambda}$. Surprisingly, while steady flow is observed exclusively for $\theta \in (\delta_{1,\lambda}, \delta_{2,\lambda})$ when $\lambda = 1$, the range of angles associated with steady flow for smoother chutes (*i.e.*, when $\lambda < 1$) extends to greater inclinations with $\theta > \delta_{2,\lambda}$. For these latter cases, $\delta_{acc,\lambda} > \delta_{2,\lambda}$ is defined as the smallest angle at which accelerating flow is observed; the DPM simulations show that

$$\delta_{acc,\lambda} = 29^\circ \pm 1^\circ \text{ for } \lambda \geq 1/2. \quad (46)$$

We summarise the density profiles seen without explicitly showing the results. For decreasing basal roughness λ , we observe that the microscopic oscillations and the dip in density at the base increase, while the bulk density remains

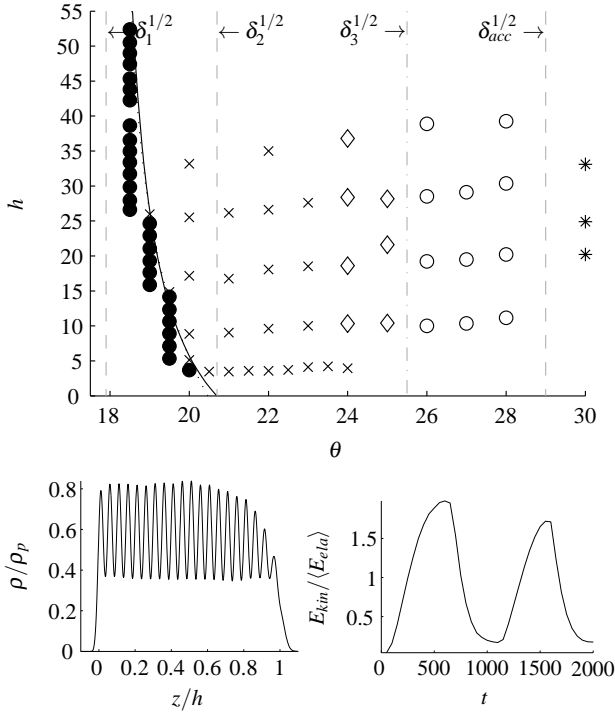


Fig. 9: Top: Overview of DPM simulations for $\lambda = 1/2$, with markers denoting the flow state at $t = 2000$: arrested \bullet , layered \times , oscillating \diamond , steady \circ , and accelerating $*$ flows. Demarcation line $h_{stop}(\theta; 1/2)$ is fitted according to (45). Bottom left panel: Profile of particle volume fraction of layered flow at $N_f/200 = 20$, $\theta = 22^\circ$. Bottom right panel: Ratio of kinetic over mean elastic energy for oscillating flow at $N_f/200 = 30$, $\theta = 24^\circ$.

constant. For $\lambda \geq 1.5$ there is a low density in the basal region, since some of the free particles are small enough to

λ	$\delta_{1,\lambda}$	$\delta_{2,\lambda}$	A_λ	β_λ	γ_λ	err
0	11.750	11.750	—	1.446	3.394	0.285
1/6	14.750	14.750	—			
1/3	16.344	20.591	23.000			
1/2	17.898	20.697	16.970	0.241	0.889	0.394
2/3	17.767	26.107	5.692	0.210	0.239	0.142
5/6	18.223	28.479	4.411	0.194	-0.002	0.144
1	17.561	32.257	3.836	0.191	-0.045	0.144
1.5	17.539	32.926	3.685	0.188	-0.036	0.147
2	17.448	29.483	5.455	0.185	-0.033	0.153
4	17.346	28.605	6.630	0.180	-0.016	0.161

Table 1: Table of fitting parameters $\delta_{1,\lambda}$, $\delta_{2,\lambda}$, A_λ for the curve $h_{stop}(\theta; \lambda)$ and β_λ , γ_λ for the flow rule (48), including the variance of the flow rule, $\text{err}(F - F_{data})$ (F is the Froude number fit and F_{data} is the measured one), for all steady ($\lambda \geq 1/2$) flows ($\lambda = 0$).

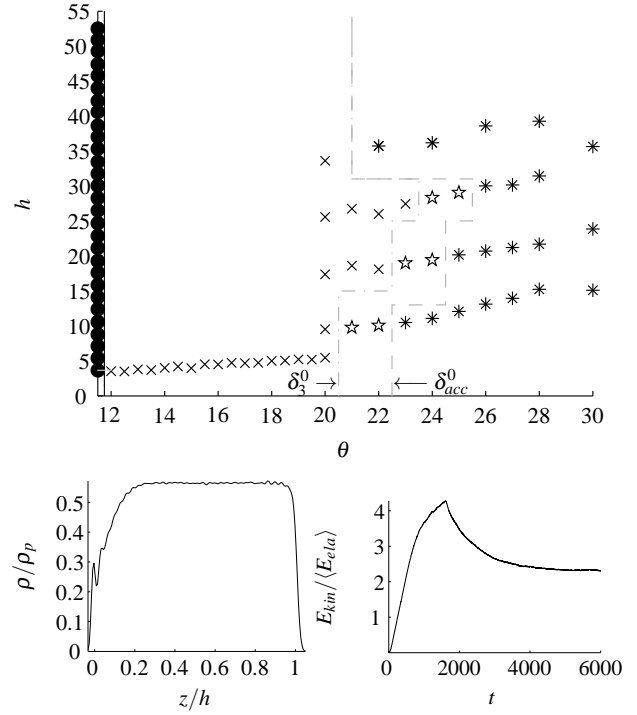


Fig. 10: Top: Overview of DPM simulations for $\lambda = 0$, with markers denoting arrested \bullet , layered \times , steady disordered $*$, and accelerating $*$ flows at $t = 2000$ ($t = 6000$ for steady disordered flows). Bottom panel: Profile of particle volume fraction (left) and ratio of kinetic over mean elastic energy (right) for $N_f/200 = 30$, $\theta = 24^\circ$.

sink a little into the base, forming a mixed layer of fixed and free particles.

Velocity profiles for $N_f/200 = 30$ and $\theta = 24^\circ$ ($\theta = 22^\circ$ and 26° for $\lambda = 1/2$) are shown for varying basal roughness in Fig. 11. For $\lambda = 1$, we observe the Bagnold profile [Bag54] for thick collisional flows, differing only at the surface. For very thin flows ($N_f/200 = 10$) or inclinations near the arresting flow regime, the profile differs strongly from the Bagnold profile and becomes linear. For smoother bases, the flow velocity increases, and the profile becomes more concave. Weak to stronger slip velocities are observed for $\lambda < 2/3$. For $\lambda = 0$, thicker flows have constant velocity throughout the depth, almost corresponding to plug flow.

For $\lambda \leq 2/3$, the flow is steady-layered and oscillating at low angles $\theta < \delta_{3,\lambda}$, where

$$\delta_{3,\lambda} = \begin{cases} 25.5^\circ \pm 0.5^\circ & \text{if } \lambda = 1/2, \\ 24.5^\circ \pm 0.5^\circ & \text{if } \lambda = 2/3 \text{ and } N_f/200 = 10, \\ \theta_{stop}(h; \lambda) & \text{if } \lambda = 2/3, N_f/200 \geq 20 \text{ or } \lambda \geq 5/6. \end{cases} \quad (47)$$

At higher angles, $\delta_{3,1/2} < \theta < \delta_{acc,1/2}$, a disordered regime similar to that for a rough base is observed. This is il-

illustrated in Fig. 9 for $\lambda = 1/2$, where one observes the two different steady state regimes. At smaller angles, $\delta_{1,1/2} < \theta < \delta_{3,1/2}$, the flowing system self-organizes into a state of layered flow consisting of ordering in the x - y -plane for the bulk (bottom left panel of Fig. 9), except for a small intermediate region, $\theta \approx \delta_{3,1/2}$, where a transitional flow regime can be found. It is characterised by large oscillations in the ratio of bulk averaged kinetic to elastic energy due to a spontaneous ordering and disordering, or stop-and-go flow, of the system as a function of time (lower right panel). The same flow regimes have been observed in [SGPL02], where the smoother bottoms were achieved by arranging the base particles in a grid-like fashion. In contrast, we always use a fully disordered base and vary the roughness by changing the basal particle size λd .

We also observe steady flows for $\lambda = 0$ as the contact friction is nonzero, see Fig. 10. While most of these flows are layered flows, a narrow regime of disordered steady flows is observed between the steady layered flows and the accelerating cases. Unlike the steady disordered flows observed for rough bases $\lambda \geq 1/2$, these steady disordered flows initially accelerate, then retard towards a steady state. As these flows are not steady at $t = 2000$, they are simulated until $t = 6000$ to ensure that a steady state is reached. The density and velocity profiles (see Figs. 10 and 11) of these flows are very similar to the supported regime that has been observed for flows over nearly smooth bases in [TRJD07] and hence is expected to be unstable if the chute angle, θ , is perturbed.

9 Closure relations for the depth-averaged model

The goal of this section is to close the shallow-layer equations (34) by a determination of the basal friction μ , the mean density $\bar{\rho}$, the stress ratio K , and the velocity profile α , using our DPMs. Additionally, we will determine the flow regimes for which such time-independent closure relations in terms of the flow variables cannot be obtained.

9.1 Friction μ in the shallow-layer model

For the rough base several friction laws have been proposed, as detailed in Section 4.2. In the following, we will compare these friction laws for the base roughness of one particle diameter, $\lambda = 1$, as well as for other ratios λ .

To obtain a function for the basal friction μ , we used the approach of Pouliquen, who found that for a rough base the Froude number is a linear function of $h/h_{stop}(\theta)$. A first approach was to fit the Froude number to a linear function of $h/h_{stop}(\theta; \lambda)$ across the range of non-accelerating DPMs. While this does work for $\lambda \geq 5/6$, a (linear or other) fit does not work well for $\lambda \leq 2/3$ because for the smoother bases steady flows occur for inclinations $\theta > \delta_{2,\lambda}$, for which

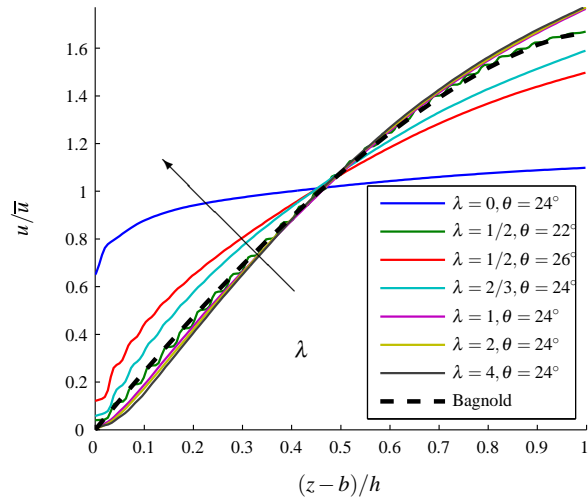


Fig. 11: Flow velocity profile of thick flow for $N_f/200 = 30$, $\theta = 24^\circ$, $\lambda = 0$ and $\lambda \geq 2/3$ and $\theta = 22^\circ, 26^\circ$, for $\lambda = 1/2$. For a rough base with $\lambda \geq 5/6$, we see a Bagnold velocity profile (dashed line), except near the surface. For smooth bases with $\lambda \leq 2/3$, the profile becomes more convex. For $\lambda = 1/2$, $\theta < 24^\circ$, the flow velocity shows layering while still observing the Bagnold profile. For $\lambda = 0$, a considerable slip velocity is observed. For $\lambda \geq 1.5$, the basal shear is small due to flow particles trapped between basal particles so that the definition of the base $b(x)$ is rather fuzzy.

$h_{stop}(\theta; \lambda)$ is not defined. This is illustrated for $\lambda = 1/2$ in Fig. 9. Instead, the Froude number is fitted with $h_{stop}(\theta; \lambda = 1)$ such that

$$F = \beta_\lambda \frac{h}{h_{stop}(\theta, \lambda = 1)} - \gamma_\lambda, \quad \text{for } \delta_{3,\lambda} < \theta < \delta_{acc,\lambda}. \quad (48)$$

The results of such fits to the Pouliquen law are shown in Fig. 12 (right), with corresponding fitting parameters provided in Table 1. Shown is the Froude number $F = \bar{u}/\sqrt{g \cos \theta h}$ against the ratio of flow and stopping heights $h/h_{stop}(\theta; \lambda = 1)$, for the disordered steady flow regime, concerning angles $\delta_{3,\lambda} < \theta < \delta_{acc,\lambda}$. Even for the inclinations where a linear fit against $h/h_{stop}(\theta; \lambda)$ is possible, the data are seen to fit better using the stopping height $h_{stop}(\theta; \lambda = 1)$, the one for basal surface $\lambda = 1$, rather than with the actual stopping height $h_{stop}(\theta; \lambda \neq 1)$. This is a key observation.

It further shows that the Froude number F increases as the roughness λ decreases, due to the lower resistance at the base. The weaker Froude number dependence for $\lambda \geq 1.5$ seen in the right panel of Fig. 12 is in line with the zero slip observed at the base in Fig. 11. The full set of fitting parameters and the standard error for the fit to (48) are found in Table 1 with a standard error defined by

$$\text{err}(\{x_i\}_{i=1}^N) = \left(\sum_{i=1}^N x_i^2 / (N-1) \right)^{1/2}. \quad (49)$$

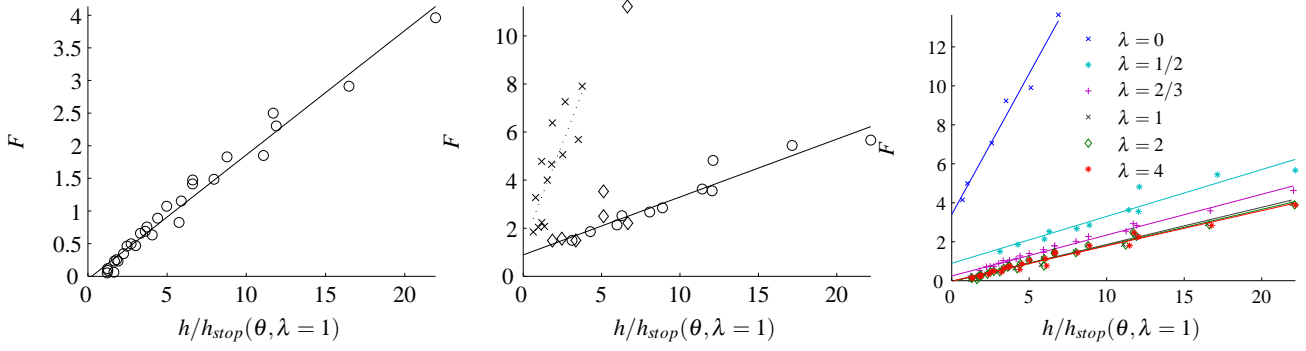


Fig. 12: Froude number $F = u/\sqrt{gh}$ over height for $\lambda = 1$ (left), $\lambda = 1/2$ (centre), scaled by the stopping height $h_{stop}(\theta; \lambda = 1)$, and for selected basal roughnesses (right). Data with symbols ‘ \times ’ denote steady layered, ‘ \circ ’ steady, and ‘ \diamond ’ oscillating flows. The data is fit using $h_{stop}(\theta, \lambda = 1)$ (solid lines).

We remark that a fit to equation (36) is marginally better than Jenkins’ adaption (40), but the differences are too small to discriminate accurately.

The situation for layered and oscillating flows is more complicated. We illustrate that for the case $\lambda = 1/2$. Two fits are shown in Fig. 12 (centre), one for the layered case (dotted line concerning the crosses), and one for the steady case (solid line concerning the circles). The oscillating flows seem to defy a sensible fit because the flow swings irregularly between the layered and disordered states. That oscillating behaviour was also shown in Fig. 9 (bottom right panel).

For steady flow, the shallow-layer equations (34) yield $\mu = \tan(\theta)$. In summary, for the steady flow regimes observed in our DPM simulations, the friction coefficient of the depth-averaged equations (34) is parameterised to be

$$\mu(h, F; \lambda) = \tan(\delta_{1,1}) + \frac{\tan(\delta_{2,1}) - \tan(\delta_{1,1})}{\beta_\lambda h / (A_1 d (F + \gamma_\lambda)) + 1}, \quad (50)$$

for $\delta_{3,\lambda} < \theta < \delta_{acc,\lambda}$, where the parameters $\delta_{1,1}$, $\delta_{2,1}$, A_1 are independent of the base; and, β_λ and γ_λ are depending explicitly on λ . All values are found in Table 1, with $\delta_{acc,\lambda}$ and $\delta_{3,\lambda}$ given in (46) and (47). Despite its determination for steady flows, such a closure for μ is assumed and often observed to be a reasonable ‘leading order’ approach for unsteady shallow-layer flows. Furthermore, for smoother bases, closure laws for layered and oscillating flows have eluded us. It seems that the homogenisation and steadiness assumptions of depth-averaged shallow-layer flow break down in these cases.

9.2 Functions $\bar{\rho}$, K , α of shallow-layer model

DPM simulations of steady uniform flows are considered for disordered steady flow with $\delta_3^\lambda < \theta \leq \delta_{acc}^\lambda$, to determine closures for $\bar{\rho}$, K and α as functions of continuum fields \bar{u} and

h . The layered and oscillating flow regimes are thus momentarily excluded.

All steady disordered flows show a constant density profile in the bulk of the flow, *cf* Fig. 6, while the density decreases near the base and the surface. The lower density region at the base spans about two particle diameters for $\lambda > 0$, while the surface region spans always less than $4d$. Thus, a mean bulk density can roughly be defined as

$$\bar{\rho}_c = \frac{1}{h - 6d} \int_{b+2d}^{s-4d} \rho(z) dz. \quad (51)$$

In Fig. 13, the bulk volume fraction and the mean volume fraction are shown for roughness $\lambda = 1$ and varying height and inclination. The bulk volume fraction decreases with inclination θ , but is independent of flow height and roughness, whereas the mean volume fraction depends also on flow height and roughness. We fit the mean bulk density of all steady disordered flows with $\lambda > 0$ to an arbitrary function

$$\bar{\rho}_c^{fit} / \rho_p = c_0 - \exp((\theta - c_2) / c_1), \quad (52a)$$

with fitting parameters

$$c_0 = 0.610, c_1 = 7.02^\circ, \text{ and } c_2 = 46.2^\circ. \quad (52b)$$

Standard deviations of the mean bulk volume fraction and mean volume fraction for all cases with $\lambda > 0$ are

$$\text{err}(\bar{\rho}_c^{fit} - \bar{\rho}_c) = 0.002, \quad \text{and} \quad \text{err}(\bar{\rho}_c^{fit} - \rho) = 0.018. \quad (52c)$$

Secondly, the normal stress ratios $K = \bar{\sigma}_{xx} / \bar{\sigma}_{zz}$ and $K' = \bar{\sigma}_{yy} / \bar{\sigma}_{zz}$ are determined. They describe the anisotropy of the stress tensor and are expected to be unity under isotropic and Newtonian conditions. The range of K for steady disordered flow is generally small, ranging from 0.98 to 1.07. The range of K' is also small, but significantly far from unity, ranging from 0.80 to 0.90.

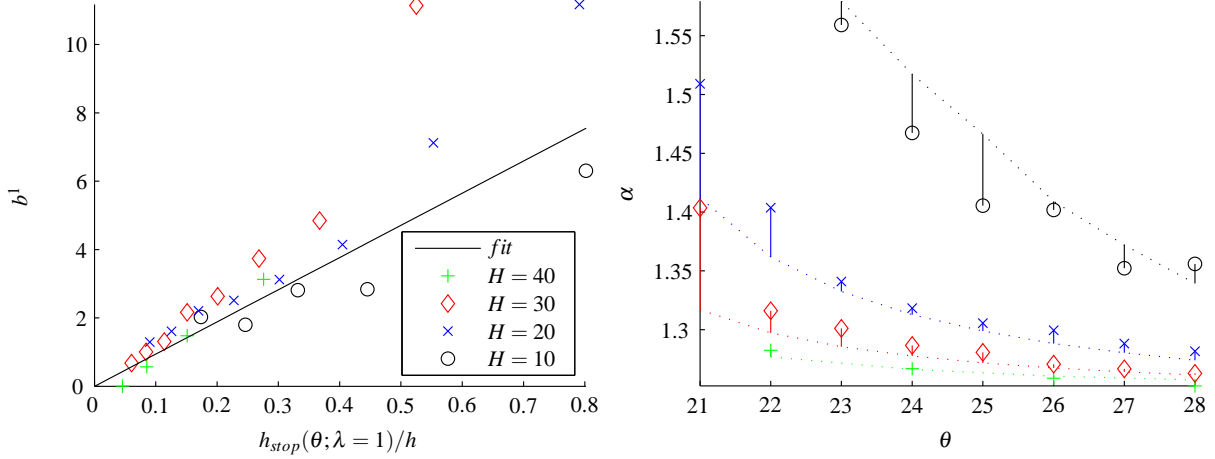


Fig. 14: Left figure: fitting parameter b_λ as a function of $h_{stop}(\theta; 1)/h$ for $\lambda = 1$ and varying height h and inclination θ . The solid line shows the linear fit used to obtain α from equations (55). Right: Shape factor α for $\lambda = 1$ and varying height h and inclination θ . Markers denote the simulation data, while dotted lines denote fits using (55) with corresponding coefficients from Table 2. Fitted values and simulation data are connected by a solid line.

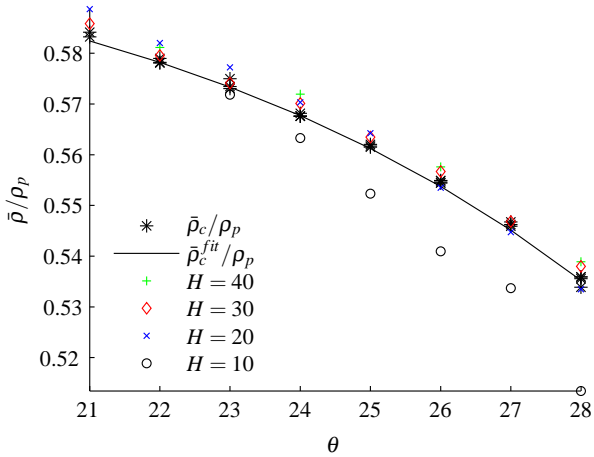


Fig. 13: Mean volume fraction $\bar{\rho}/\rho_p$ for roughness $\lambda = 1$, and varying number of particles N_f and inclinations θ . The mean volume fraction in the bulk, $\bar{\rho}/\rho_p$, denoted by *, collapses onto a function of the inclination (solid line), while it shows a small dependence on the flow height, due to the density decrease near base and surface.

The deviation of K and K' from unity increases with inclination, with K increasing and K' decreasing with inclination. This implies that the flow is contracting in one direction and expanding in the other. For steady disordered flows, K and K' fit to functions linear in θ ,

$$K^{fit} = 1 + (\theta - d_1)/d_0 \quad (53)$$

with $d_0 = 132^\circ$ and $d_1 = 21.30^\circ$ and

$$K'^{fit} = 1 + (\theta - d'_1)/d'_0 \quad (54)$$

with $d'_0 = -118^\circ$ and $d'_1 = 6.27^\circ$. The model results give a small standard error of $\text{err}(K - K^{fit}) = 0.014$ and $\text{err}(K' - K'^{fit}) = 0.014$. Given that the dependence on inclination is small, we can take $K \approx 1$, while K' does not appear in the 2D shallow-layer granular equations.

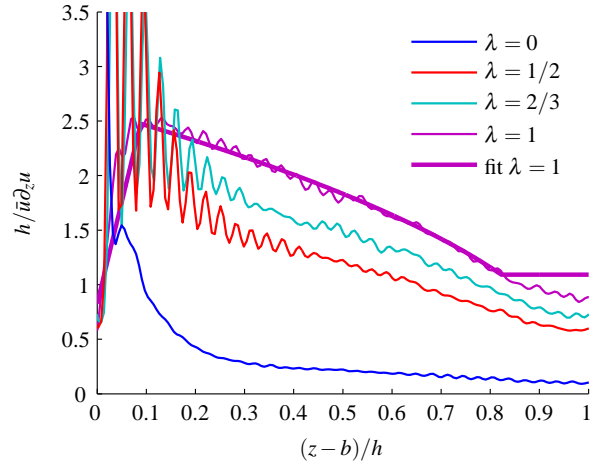


Fig. 15: Depth profile of normalised strain, $(h/\bar{u}) \partial_z u$ corresponding to velocity profiles shown in Fig. 11. For rough bases, the strain is modelled by a Bagnold profile, except near the base and surface. For smoother bases, $\lambda \leq 2/3$, the layered flow near the base increases in thickness. For $\lambda = 0$, a large slip velocity and a shear band in the basal layer is observed.

Finally, we develop a fit for the shape factor $\alpha(\lambda) = \bar{u}^2/u^2$.

The fit is based on a phenomenological model of the observed velocity profiles, as shown in Fig. 11. For rough bases $\lambda \geq 5/6$, a Bagnold velocity profile,

$$u_B(z) = \frac{5}{3} \bar{u} \left(1 - \left(\frac{h-z}{h} \right)^{3/2} \right), \quad (55a)$$

is observed in the bulk of the flow; a linear profile in the surface layer, which is about $5d$ thick; and, a convex profile with no slip in the base layer, whose thickness b_λ increases as the height approaches the stopping height. No kinks occur at the intersection of the layers. Thus, we model the velocity by

$$\frac{\partial u}{\partial z}(z; b_\lambda) = \begin{cases} \frac{\partial u_B}{\partial z}(z = b_\lambda) \left(1 - \frac{2}{3} \frac{b_\lambda - z}{b_\lambda - b} \right), & z < b_\lambda, \\ \frac{\partial u_B}{\partial z}(z), & b_\lambda \leq z < \max(s-5, b_\lambda), \\ \frac{\partial u_B}{\partial z}(z = \max(s-5, b_\lambda)), & \text{otherwise,} \end{cases}$$

$$u(0; b_\lambda) = 0 \text{ for } \lambda \geq 5/6. \quad (55b)$$

The strain $\partial_z u$ in Fig. 15 is fitted well with (55). The parameter b_λ decreases with increasing distance from the stopping height, and a simple fit reads

$$b_\lambda = d_\lambda h_{stop}(\theta, 1)/h, \quad (55c)$$

where $h_{stop}(\theta, 1)$ was chosen since $h_{stop}(\theta, \lambda)$ does not provide values for all inclinations for which steady flow is observed. Subsequently, the fit to the shape factor $\alpha(\lambda) = \bar{u}^2/\bar{u}^2$ can be computed numerically and compared to the measured values in Fig. 14. The coefficients b_λ are given in Table 2.

For $\lambda \leq 2/3$, the dependence of the shape factor on height and inclination diminishes and can be approximated with a constant value $\alpha(\lambda)$. The Bagnold profile disappears and the flow becomes more convex and plug-like, as shown in Fig. 11. Each velocity profile will be analysed separately next.

For $\lambda = 0$, the slip is so large that we can assume plug flow to hold. There is almost no slip for $\lambda = 2/3$ and a slip of approximately $u(0)/\max_z u(z) = 1/6$ for $\lambda = 1/2$. We neglect the variations at the surface and the bulk and assume a linear shear rate vanishing at the surface for $\lambda = 1/2$, $\lambda = 2/3$. Thus, we fit the velocity profiles as

$$\frac{u(z)}{\bar{u}} = \begin{cases} z/h(2-z/h), & \lambda = 2/3, \\ 0.16 + 0.84(z/h(2-z/h)), & \lambda = 1/2, \\ 1, & \lambda = 0, \end{cases} \quad (56)$$

The corresponding coefficients $\alpha(\lambda)$ are found in Table 2 and provide a good fit to the data.

The Bagnold velocity profile in the bulk region can be deduced, without assuming collisional flow, from a local rheology model [GDR04] where it is assumed that the friction μ is a function of the inertial number,

$$I(z) = (\partial_z u_x) / \left(\sqrt{\sigma_{zz}/\rho_p/d} \right). \quad (57)$$

λ	$\alpha(\lambda)$	err
0	1.00	0.0027
1/2	1.14	0.022
2/3	1.20	0.014

λ	b_λ	err
5/6	5.37	0.0371
1	9.42	0.0395
3/2	9.69	0.0239
2	12.0	0.0473
4	14.5	0.0543

Table 2: Fitting for the shape factor $\alpha = \alpha(\lambda)$ for $\lambda \leq 2/3$ and $\alpha = \bar{u}^2/\bar{u}^2$, $u = u(z; b_\lambda)$ for $\lambda \geq 5/6$, and the standard error. Closure relations are fitted to all data sets of steady unordered flow, $\delta_3^\lambda < \theta \leq \delta_{acc}^\lambda$.

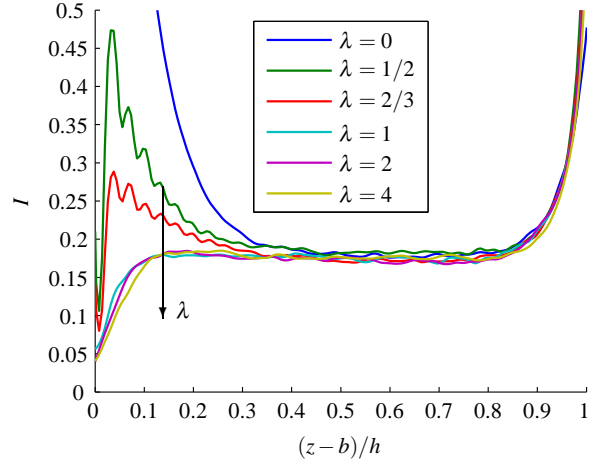


Fig. 16: Inertial number $I(z)$ for $N_f/200 = 30$ at inclination $\theta = 25^\circ$ for varying roughness λ . The basal region shows large variations in I which increase for smoother bases.

Since the friction is determined by the inclination, $\mu = \tan(\theta)$, we thus expect a constant value of I in the bulk. Depth profiles of I are plotted in Fig. 16 for varying roughnesses λ . The inertial number remains constant in the bulk, but shows large variations in the basal and surface layers. At the surface, the pressure vanishes while the strain rate remains finite (see Fig. 11), causing the inertial number to approach infinity. At the base we observe different behaviour for rough and for smooth basal surfaces. For high geometric roughness, $\lambda > 2/3$, the inertial number increases towards the base, reflecting the decrease in strain rate previously shown in Fig. 15. For smoother bases $\lambda \leq 2/3$, the basal region is thicker and the inertial number increases towards the base. For $\lambda = 0$, the inertial number reaches such high values that the flow needs to be classed as collisional, which is confirmed by the density profile for the steady disordered cases, as shown in Fig. 10.

Assuming that the $\mu(I)$ -rheology holds, the velocity should fit a Bagnold profile and therefore we expect a constant shape factor $\alpha = 5/4$. As both density and friction depend only on the inertial number, a further prediction is that the density is a function of the friction, $\bar{\rho} = \bar{\rho}(\mu = \tan \theta)$, in agreement

with the density fit in equation (52). In [GDR04], it was further assumed that $K = 1$. The friction can also be expressed in terms of the inertial number: due to the Bagnold velocity profile, the inertial number of the flow can be modeled in terms of the flow variables as

$$\bar{I} = \frac{5}{2} \frac{\bar{u}d}{h\sqrt{gh\cos\theta}} = \frac{5Fd}{2h}, \quad (58)$$

where we use the notation \bar{I} to distinguish from the definition of the local inertial number (57). From (58) it immediately follows that the Froude number is proportional to the height, without an offset as assumed in (48). We note that the $\mu(\bar{I})$ -rheology does not predict a height dependent stopping angle, $\theta_{stop}(h)$, as is observed in the simulations: since $\mu = \mu(\bar{I})$, there is also an inverse function $\bar{I} = \bar{I}(\mu = \tan\theta)$, therefore \bar{I} is independent of the height of the flow. Instead there is a single minimal angle, $\theta_{1,\lambda}$, for which steady flows exist. In order to obtain a fit, we assume that steady flow is not possible above an angle $\theta_{max,\lambda}$ and fit $\mu(\bar{I})$ as

$$\mu(\bar{I}) = \tan(\delta_{1,\lambda}) + \frac{\tan(\delta_{max,\lambda}) - \tan(\delta_{1,\lambda})}{(a_\lambda \bar{I})^{-1} + 1} \quad (59)$$

with fitting parameters $\delta_{max,\lambda}$ and a_λ given in Table 3. This fit is similar to the fit obtained in (50), except that $\mu(\bar{I})$ is now fitted directly. For $\lambda \geq 5/6$, μ shows a well-defined dependence of \bar{I} ; however, this functional dependence vanishes for smoother bases $\lambda \leq 2/3$, as the flow velocity becomes less Bagnold-like, see Figure 11, and the offset from a linear relationship between F and h increases, see Figure 12.

These deviations from the $\mu(I)$ -rheology for a rough base have also been observed in [GDR04]; consequently, a non-local rheology has been proposed by Pouliquen and Forterre in [PF09], where rearrangements at one position are triggered by stress fluctuations elsewhere in the flow. This non-local rheology predicts for rough bases that the bulk flow is

λ	a_λ	$\theta_{1,\lambda}$	$\theta_{max,\lambda}$	err_1	err_2
0	0.0008	11.8	89.8	0.013	0.0025
1/2	2.11	17.9	36.8	0.0054	0.0026
2/3	3.45	17.8	35.9	0.0016	0.0031
5/6	5.25	18.2	34.4	0.0022	0.0026
1	7.2	17.6	33.3	0.0034	0.0025
1.5	7.17	17.5	33.4	0.0034	0.0025
2	7.25	17.4	33.5	0.0033	0.0025
4	6.22	18	34.3	0.0031	0.0027

Table 3: Table of fitting parameters a_λ and $\theta_{max,\lambda}$, as well as the previously measured angle of repose, $\theta_{1,\lambda}$. For $\lambda = 0$, the fitting returns an almost linear fit to the data.

The last two columns show the variance of the friction fitted by equation (59), $err_1 = (N - 1)^{-1} \sum_{i=1}^N (\mu(\bar{I}) - \tan(\theta))^2$, and fitted by equation (50), $err_2 = (N - 1)^{-1} \sum_{i=1}^N (\mu(h, F) - \tan(\theta))^2$.

Bagnold, while the strain rate remains finite at the surface, and decreases towards the base. This is in qualitative agreement with what we observe in our DPM simulations, see Figs. 11 and 15. However, this non-local rheology could not predict other observed details, such as the inverse proportionality of the Froude number on the stopping height, see (48).

In summary, the functions $\bar{\rho}$, α and K depend on the inclination θ and the height h . The inclination θ in turn can be written as a function of the friction coefficient μ such that $\theta = \tan^{-1}(\mu(h, \bar{u}))$. This allows us to describe the parameters of the shallow-layer model in terms of the height h , roughness λ , and friction $\mu(h, \bar{u})$ and thus provides a closure proper for the system. The different behavior for the varying λ 's remains an open issue, since we only provided empirical fits above.

10 Conclusion

10.1 Summary

In this article, an extensive series of DPM simulations were used to determine closure relations for the often used shallow-layer model of granular flows on inclined chutes. Assuming uniformity in the lateral y -direction, the model is a depth-averaged continuum model with the macro-scale variables thickness $h = h(x, t)$ and mean velocity $\bar{u} = \bar{u}(x, t)$. The flow consisted of monodispersed particles of diameter d and the base of monodispersed particles of diameter λd . Particle flows with variations in height h and inclination θ were numerically investigated for varying basal roughness λ , revealing a range of parameters for which steady and uniform flow was observed.

We observed the following phenomenology: at small inclinations the flow quickly arrests, while at large inclinations the flow continues to accelerate. Between these two regimes there was a range of inclinations in which steady flows occurred (*cf.* Fig. 4). The curve $h_{stop}(\theta; \lambda)$, a function of height versus inclination, forms the demarcation between arrested and steady flow, as a function of basal roughness (Figs. 4 and 8). For smaller basal roughness, steady states arise at smaller inclinations and heights, and the range of angles shrinks for which steady flow is possible. Other types of steady flow were observed at small inclinations for small base particles, showing a strong layering in depth, or oscillatory flows (*cf.* Fig. 9). For a flat frictional base, the steady disordered flows show a strong shear at the base.

Depth profiles for density, velocity and stress were constructed using coarse-grained macroscopic fields. The coarse-graining width was carefully chosen to preserve some microscopic structure as well as macroscopic gradients (*cf.* Fig. 6). The assumptions of depth-averaged theory were confirmed in the simulations for a certain range of steady, uniform

flows: the density was almost constant with depth, and the downward normal stress as well as shear stress were lithostatic. We have only derived closure relations from statistically steady DPM simulations; however, it is often assumed that such closure laws, obtained from either DPM simulations or experiments, can be used to close the time-dependent granular shallow-layer equations.

Consequently, four closure relations could be determined: basal friction μ , stress ratio K , mean density $\bar{\rho}$, and the shape of the velocity profile α .

Firstly, basal friction $\mu = \tan \theta$ was shown to be a function of height and flow velocity, see Eq. (50). Pouliquen’s approach was found to be valid for $\lambda = 1$, with the Froude number as a linear function of $h/h_{stop}(\theta; \lambda = 1)$. This fitting approach was extended to smoother bases with $\lambda \neq 1$, where the Froude number was fitted to $h/h_{stop}(\theta; \lambda = 1)$ instead of using the respective $h/h_{stop}(\theta; \lambda)$ for the actual λ or basal roughness. The stopping curve associated with the diameter $\lambda d = 1$ of the flowing particles seems more relevant than the stopping height with the actual λ . One possible explanation is that there is a boundary layer of intermittently slow flow particles that originated in the bulk, and that shields the smoother base from the bulk flow.

Secondly, closure relations for the mean density $\bar{\rho}$, stress anisotropy K and shape factor α were established as follows. The mean density was fitted as a decreasing function of inclination, see Eq. (52); the stress anisotropy was found to be increasing with inclination, but the variations were small enough to assume $K \approx 1$; the shape factor was obtained by fitting the velocity profiles at the base with a convex function, a Bagnold profile in the bulk, and linear profile at the base, with the base height proportional to $h_{stop}(\theta; \lambda = 1)$.

The determined closures are valid for the range of inclinations $\delta_{3,\lambda} < \theta < \delta_{acc,\lambda}$, where steady disordered flows are observed. For rough bases with $\lambda \geq 5/6$, all steady flows were disordered, and therefore $\delta_{3,\lambda} = \theta_{stop}(h; \lambda)$, with $\theta_{stop}(h; \lambda)$ the inverse of the $h_{stop}(\theta; \lambda)$ -curve between arrested and dynamic flow. For smaller roughness with $\lambda \leq 2/3$, layered and oscillating flows arose for inclinations $\theta_{stop}(h; \lambda) < \theta < \delta_{3,\lambda}$, for which we are (as yet) unable to capture closure relations.

10.2 Open questions

What does the granular shallow-layer model enable us to do, and what can we not do with it? In the range of steady flows, this continuum model can be used to predict steady and time-dependent flows. Strictly speaking, this is only allowed for steady flow in the established inclination range $\delta_{3,\lambda} < \theta < \delta_{acc,\lambda}$, but it can be expected to remain valid for the slowly-varying dynamic cases as well. It is often the case, however, that even rapidly-changing flows can be cap-

tured by models that are strictly only valid for the slowly-varying cases. Consequently, a systematic study of the validity of the granular shallow-layer model is required. By respectively extending the “hydraulic” analysis for fluidised granular matter and water in Vreman *et al.* [VATK⁺07] and Akers and Bokhove [AB08], granular flows within constrictions become an analytically-treatable target. Such flows in constrictions reach a steady state and appear (partially) accessible by direct DPM simulations.

What do these results enable us to do? Whether the steady DPM-based closures are valid across granular “hydraulic” jumps in such steady and constricted flows is of interest. Whether the steady DPM-based closures hold for (slow) transient routes towards such steady states is of interest, too. What closures should be used outside the formal range of applicability for the smoother bases, so for the layered and oscillating flows for $\theta_{stop}(h; \lambda) < \theta < \delta_{3,\lambda}$ and the accelerating flows for $\theta > \delta_{acc,\lambda}$, appears a tantalising, and as yet, open question.

What are we not able to do? Although, we did observe layered and oscillating flows in our DPM simulations, it is doubtful whether the homogenisation assumption that led to the shallow-layer model is sufficient. Nonetheless, the lithostatic balance relation is shown to hold for the DPM simulations, as expected from standard asymptotic analysis using the aspect ratio of normal to planar velocity and length scales.

10.3 Outlook

Alternatively, a multi-scale modelling approach might be adopted such as the heterogeneous, multiscale methodology [WEL⁺07], among others, in which closure relations for discretisations (*e.g.*, [PBS⁺07]) depth-averaged shallow-layer models are coupled to DPM simulations in selected regions in space and time. Thus computational costs would be diminished while accurate closure relations are gathered ‘on the fly’ in time and space.

For future work, we advocate the extension of our DPM simulations by investigating the three-dimensional closure relations. We surmise that reduced lithostatic models for shallow granular flows could be more consistently derived from three-dimensional continuum models with stress closures determined from DPM simulations in combination with laboratory measurements. These new models would be reduced and therefore computationally still manageable for large-scale debris flows; for example, when the degrees of freedom in the vertical remain limited, but are extended beyond only one degree of freedom. Such reduced modelling is akin to hydrostatic modelling in water-wave and coastal hydrodynamics.

References

- [AB08] B. Akers and O. Bokhove. Hydraulic flow through a contraction: multiple steady states. *Phys. Fluids*, 20:056601, 2008.
- [AT93] M.P. Allen and D.J. Tildesley, editors. *Computer Simulation of Liquids*. Oxford University Press, 1993.
- [Bab97] Marijan Babic. Average balance equations for granular materials. *Int. J. Eng. Science*, 35(5):523–548, 1997.
- [Bag54] R.A. Bagnold. Experiments on a gravity-free dispersion of large spheres in a newtonian fluid under shear. *Proc. Roy. Soc. A*, 255:49–63, 1954.
- [BE06] T. Borzsonyi and R.E. Ecke. Rapid granular flows on a rough incline: Phase diagram, gas transition, and effects of air drag. *Phys. Rev. E*, 74(6):9, 2006.
- [BE07] T. Borzsonyi and R.E. Ecke. Flow rule of dense granular flows down a rough incline. *Phys. Rev. E*, 76(3):10, 2007.
- [BT12] O. Bokhove and A.R. Thornton. Shallow granular flows. In H.J. Fernando, editor, *Handbook of Environmental Fluid Dynamics*. CRC Press, 2012.
- [CGJ07] X. Cui, J.M.N.T. Gray, and T. Johannesson. Deflecting dams and the formation of oblique shocks in snow avalanches at flateyri. *J. Geophys. Res.*, 112, 2007.
- [CS79] P.A. Cundall and O.D.L. Strack. A discrete numerical model for granular assemblies. *Geotechnique*, 29(4765), 1979.
- [DD99] A. Daerr and S. Douady. Two types of avalanche behaviour in granular media. *Nature*, 399(6733):241–243, 1999.
- [DI01] R.P. Denlinger and R.M. Iverson. Flow of variably fluidized granular masses across three-dimensional terrain 2. numerical predictions and experimental tests. *J. Geophys. Res.*, 106(B1):533–566, 2001.
- [DPP⁺08] K. Dalbey, A.K. Patra, E.B. Pitman, M.I. Bursik, and M.F. Sheridan. Input uncertainty propagation methods and hazard mapping of geophysical mass flows. *J. Geophys. Res.*, 113, 2008.
- [FP03] Y. Forterre and O. Pouliquen. Long-surface-wave instability in dense granular flows. *J. Fluid Mech.*, 486:21–50, 2003.
- [GC07] J.M.N.T. Gray and X. Cui. Weak, strong and detached oblique shocks in gravity driven granular free-surface flows. *J. Fluid Mech.*, 579:113–136, 2007.
- [GDDT07] C. Goujon, B. Dalloz-Dubrujeaud, and N. Thomas. Bidisperse granular avalanches on inclined planes: A rich variety of behaviors. *Eur. Phys. J. E.*, 23(2):199–215, 2007.
- [GDR04] GDR MiDi. On dense granular flows. *Eur. Phys. J. E.*, 14:341–365, 2004.
- [GEY67] S.S. Grigorian, M.E. Eglit, and Y. L. Yakimov. New statement and solution of the problem of the motion of snow avalanches. *Physics of Snow, Avalanches and Glaciers, Tr Vysokogornogo Geofizich Inst.*, 12, 1967.
- [Gol10] I. Goldhirsch. Stress, stress asymmetry and couple stress: from discrete particles to continuous fields. *Granular Matter*, 12(3):239–252, 2010.
- [GTDD03] C. Goujon, N. Thomas, and B. Dalloz-Dubrujeaud. Monodisperse dry granular flows on inclined planes; role of roughness. *Eur. Phys. J. E.*, 11:147–157, 2003.
- [GTN03] J.M.N.T. Gray, Y.C. Tai, and S. Noelle. Shock waves, dead zones and particle-free regions in rapid granular free surface flows. *J. Fluid Mech.*, 491:161–181, 2003.
- [GWH99] J.M.N.T. Gray, M. Wieland, and K. Hutter. Free surface flow of cohesionless granular avalanches over complex basal topography. *Proc. Roy. Soc. A*, 455:1841–1874, 1999.
- [HH05] K.M. Hákonardóttir and A.J. Hogg. Oblique shocks in rapid granular flows. *Phys. Fluids*, 17, 2005.
- [HM84] O. Hungr and N.R. Morgenstern. Experiments on the flow behaviour of granular materials at high velocity in an open channel. *Geotechnique*, 34:415–421, 1984.
- [HSSN93] K. Hutter, M. Siegel, S.B. Savage, and Y. Nohguchi. Two-dimensional spreading of a granular avalanche down an inclined plane. 1. theory. *Acta Mech.*, 100(1-2):37–68, 1993.
- [IK50] J.H. Irving and J.G. Kirkwood. The statistical mechanical theory of transport processes. *J. Chem. Phys.*, 18:817, 1950.
- [Ive97] R.M. Iverson. The physics of debris flows. *Rev. Geophys.*, 35:245–296, 1997.
- [JB10] J.T. Jenkins and D. Berzi. Dense inclined flows of inelastic spheres: tests of an extension of kinetic theory. *Granular Matter*, 12, 2010.
- [Jen93] J.T. Jenkins. Hydraulic theory for a debris flow supported on a collisional shear layer. In *Proc. Int. Congress on Hydraulics Research IAHR, Tokyo*, pages 1–12, 1993.
- [Jen06] J.T. Jenkins. Dense shearing flows of inelastic disks. *Phys. Fluids*, 18, 2006.
- [Jen07] J.T. Jenkins. Dense inclined flows of inelastic spheres. *Granular Matter*, 10:47–52, 2007.
- [KE73] A.G. Kulikovskii and M.E. Eglit. Two-dimensional problem of the motion of a snow avalanche along a slope with smoothly changing properties. *Prikladnaya Matematika i Mekhanika*, 37(5):837–848, 1973.
- [LK01] M.Y. Louge and S.C. Keast. On dense granular flows down flat frictional inclines. *Phys. Fluids*, 13(5), 2001.
- [LLV⁺01] S. Luding, M. Lätzel, W. Volk, S. Diebels, and H.J. Herrmann. From discrete element simulations to a continuum model. *Comp. Meth. Appl. Mech. Engng.*, 191(21–28), 2001.
- [Lou03] M.Y. Louge. Model for dense granular flows down bumpy inclines. *Phys. Rev. E*, 67(061303), 2003.
- [Lud04] S. Luding. Micro-macro models for anisotropic granular media. In P.A. Vermeer, W. Ehlers, H.J. Herrmann, and E. Ramm, editors, *Micro-Macro Models for Anisotropic Granular Media*, pages 195–206. A.A. Balkema, Leiden, 2004.
- [Lud08] S. Luding. Introduction to discrete element methods: basics of contact force models and how to perform the micro-macro transition to continuum theory. *European J. of Environ. Civil Eng.*, 12(7-8):785–826, 2008.
- [Lud09] S. Luding. From molecular dynamics and particle simulations towards constitutive relations for continuum theory. In B. Koren and K. Vuik, editors, *Advanced Computational Methods in Science and Engineering*, Lecture Notes in Computational Science and Engineering. Springer, 2009.
- [PBS⁺07] L. Pesch, A. Bell, W.H. Sollie, V.R. Ambati, O. Bokhove, and J.J.W. Van der Vegt. hp-gem a software framework for discontinuous galerkin finite element methods. *ACM Transactions on Mathematical Software*, 33(4), 2007.
- [PF02] O. Pouliquen and Y. Forterre. Friction law for dense granular flows: application to the motion of a mass down a rough inclined plane. *J. Fluid Mech.*, 453:131–151, 2002.
- [PF09] Olivier Pouliquen and Yoel Forterre. A non-local rheology for dense granular flows. *Physical and Engineering Sciences*, 367(1909):5091–5107, December 2009.
- [Pou99] O. Pouliquen. Scaling laws in granular flows down rough inclined planes. *Phys. Fluids*, 11(3):542–548, 1999.
- [SA04] S. Shen and S.N. Atluri. Atomic-level stress calculation and continuum molecular system equivalence. *Computer Modeling in Engineering and Sciences*, 6(1):91–104, 2004.
- [SEG⁺01] L.E. Silbert, D. Ertas, G.S. Grest, D. Halsey, T.C. Levine, and S.J. Plimpton. Granular flow down an inclined plane:

- Bagnold scaling and rheology. *Phys. Rev. E.*, 64(051302), 2001.
- [SGPL02] L.E. Silbert, G.S. Grest, S.J. Plimpton, and J.W. Landry. Boundary effects and self-organization in dense granular flows. *Phys. Fluids*, 14(8), 2002.
- [SH82] P. Schofield and J.R. Henderson. Statistical mechanics of inhomogeneous fluids. *Proc. R. Soc.*, 379:231–246, 1982.
- [SH89] S.B. Savage and K. Hutter. The motion of a finite mass of material down a rough incline. *J. Fluid Mech.*, 199:177–215, 1989.
- [SLG03] L.E. Silbert, J.W. Landry, and G.S. Grest. Granular flow down a rough inclined plane: Transition between thin and thick piles. *Phys. Fluids*, 15(1):1–10, 2003.
- [TED95] B.D. Todd, D.J. Evans, and P.J. Daivis. Pressure tensor for inhomogeneous fluids. *Phys. Rev. E*, 52(2), 1995.
- [TRJD07] N. Taberlet, P. Richard, J. T. Jenkins, and R. Delannay. Density inversion in rapid granular flows: the supported regime. *The European Physical Journal E: Soft Matter and Biological Physics*, 22(1):17–24, January 2007.
- [VATK⁺07] A.W. Vreman, M. Al-Tarazi, A.M. Kuipers, M. Van Sint Annaland, and O. Bokhove. Supercritical shallow granular flow through a contraction: experiment, theory and simulation. *J. Fluid Mech.*, 578:233–269, 2007.
- [WB86] O.R. Walton and R.L. Braun. Viscosity, granular temperature, and stress calculations for shearing assemblies of inelastic, frictional disks. *J. Rheology*, 30(949), 1986.
- [WEL⁺07] E. Weinan, Bjorn Engquist, Xiantao Li, Weiqing Ren, and Eric Vanden-Eijnden. Heterogeneous Multiscale Methods: A Review. *Comm. Comput. Physics*, 2(3):367–450, June 2007.
- [WGH99] M. Wieland, J.M.N.T. Gray, and K. Hutter. Channelised free surface flow of cohesionless granular avalanches in a chute with shallow lateral curvature. *J. Fluid Mech.*, 392:73–100, 1999.
- [WSS08] R. Williams, A.J. Stinton, and M.F. Sheridan. Evaluation of the Titan 2D two-phase flow model using an actual event: Case study of the Vazcún valley lahar. *J. Volcan. Geotherm. Res.*, 177:760–766, 2008.
- [WTLB11] T. Weinhart, A.R. Thornton, S. Luding, and O. Bokhove. From discrete particles to continuum fields near a boundary. *Granular Matter*, Special volume for Goldhirsch. In press, 2011.

Acknowledgements

The authors would like to thank the Institute of Mechanics, Processes and Control, Twente (IMPACT) for the primary financial support of this work as part of the research program "Superdispersed multiphase flows". We also thank the NWO VICI grant 10828 and the DFG project SPP1482 B12 for financial support.

The DPM simulations performed for this paper are undertaken in Mercury-DPM, which was initially developed within this IMPACT program. It is primarily developed by T. Weinhart, A.R. Thornton and D. Krijnsman as a joint project between (both) the Multi Scale Mechanics (Mechanical Engineering) and the Mathematics of Computational Science (Applied Mathematics) groups at the University of Twente.

A System of Hamiltonian equations in the dissipation-free limit

The purpose of this appendix is to show that the particle system in the dissipation- and yield-free limit, *i.e.*, $\gamma^n = \gamma^t = 0$ and $\mu_c \rightarrow \infty$, is a Hamiltonian system. It subsequently facilitates the derivation of so-called conservative or symplectic discretization schemes, in time. These have been shown and are believed to provide better long-term statistics than classical time discretization schemes. Furthermore, analysis of the Hamiltonian limit allows one to clearly demarcate the transfer of energy between its kinetic, elastic, and internal components.

We show that the normal and tangential forces are elastic, that is the system does not dissipate energy; instead kinetic energy is converted into potential energy in the springs and vice versa. If the tangential spring is not fully unloaded when two particles loose contact, the potential energy stored in the tangential spring is converted into internal potential energy in each particle (vibrations).

We use the notation given in §2. In the dissipation- and yield-free limit, the contact force between particles i, j is given by

$$\mathbf{f}_{ij} = k^n \delta_{ij}^n \hat{\mathbf{n}}_{ij} - k^t \delta_{ij}^t, \quad (60)$$

where δ_{ij}^n and δ_{ij}^t are given by equations (1) and (9). The equations of motion for translational and angular momentum of particle i are given by,

$$\frac{d}{dt} \mathbf{r}_i = \mathbf{p}_i / m_i, \quad \frac{d}{dt} \alpha_i = \phi_i \quad (61a)$$

$$(61b)$$

$$\frac{d}{dt} \mathbf{p}_i = m_i \mathbf{g} + \sum_{j \neq i} \mathbf{f}_{ij}, \quad \frac{d}{dt} \phi_i = \sum_{j \neq i} \mathbf{b}_{ij} \times \mathbf{f}_{ij}, \quad (61c)$$

in three dimensions, where \mathbf{r}_i is the position, α_i is the angle, \mathbf{p}_i the momentum and ϕ_i the angular momentum of particle i .

To define the Hamiltonian system, we pair these generalized position and momentum vectors as follows

$$\mathbf{Q}(t) = \{\mathbf{r}_i(t), \alpha_i(t)\}_{i=1}^N, \quad \mathbf{P}(t) = \{\mathbf{p}_i(t), \phi_i(t)\}_{i=1}^N. \quad (62)$$

Then the kinetic energy can be calculated using only the generalized momenta \mathbf{P} as follows

$$T(\mathbf{P}) = \sum_{i=1}^N \left(\frac{|\mathbf{p}_i|^2}{2m_i} + \frac{|\phi_i|^2}{2I_i} \right). \quad (63)$$

The potential energy is a combination of the potential of gravity, the potential of the normal and tangential springs and the internal potential energy in the particles, created from the remaining potential of the tangential spring at the time t_{ij}^e that a particle pair $\{i, j\}$ looses contact,

$$\{t_{ij}^e\} = \{t : \frac{d_i + d_j}{2} - |\mathbf{r}_{ij}(t)| = 0, \frac{d}{dt} |\mathbf{r}_{ij}(t)| > 0\} \quad (64)$$

with $\mathbf{r}_{ij} = \mathbf{r}_j(t) - \mathbf{r}_i(t)$. The potential can be expressed in terms of the position and the tangential springs at all times, which itself is a function of the previous positions of the particle pair,

$$V(\mathbf{Q}) = V_{grav}(\mathbf{Q}) + V_{ela}(\mathbf{Q}) + V_{int}(\mathbf{Q}). \quad (65a)$$

where the gravitational, elastic and internally stored potential energy is defined by

$$V_{grav}(\mathbf{Q}) = \sum_{i=1}^N -m_i \mathbf{r}_i \cdot \mathbf{g} \quad (65b)$$

$$V_{ela}(\mathbf{Q}) = \sum_{i=1}^N \sum_{j=i+1}^N \left(\frac{k^n}{2} |\delta_{ij}^n|^2 + \frac{k^t}{2} |\delta_{ij}^t|^2 \right). \quad (65c)$$

$$V_{int}(\mathbf{Q}) = \sum_{i=1}^N \sum_{j=i+1}^N \sum_{t_{ij}^e < t} \left(\frac{k^t}{2} |\delta_{ij}^t(t_{ij}^e)|^2 \right). \quad (65d)$$

We will now show that the total energy $H = T + V$ satisfies the Hamiltonian equations,

$$\frac{\partial H}{\partial \mathbf{r}_i} = -\frac{d\mathbf{p}_i}{dt}, \quad \frac{\partial H}{\partial \boldsymbol{\alpha}_i} = -\frac{d\boldsymbol{\phi}_i}{dt}, \quad (66a)$$

$$\frac{\partial H}{\partial \mathbf{p}_i} = \frac{d\mathbf{r}_i}{dt}, \quad \text{and} \quad \frac{\partial H}{\partial \boldsymbol{\phi}_i} = \frac{d\boldsymbol{\alpha}_i}{dt}. \quad (66b)$$

To derive (66a), we calculate

$$\frac{\partial H}{\partial \mathbf{r}_i} = \frac{\partial}{\partial \mathbf{r}_i} \left(-m_i \mathbf{r}_i \cdot \mathbf{g} + \sum_{j \neq i} \left(\frac{k^n}{2} |\boldsymbol{\delta}_{ij}^n|^2 + \frac{k^t}{2} |\boldsymbol{\delta}_{ij}^t|^2 \right) \right) \quad (67)$$

term by term. We can show that

$$\begin{aligned} \frac{\partial}{\partial \mathbf{r}_i} \frac{k^n}{2} \boldsymbol{\delta}_{ij}^{n2} &= k^n \max(0, (d_i + d_j)/2 - r_{ij}) \frac{\partial \max(0, (d_i + d_j)/2 - r_{ij})}{\partial \mathbf{r}_i} \\ &= k^n \max(0, (d_i + d_j)/2 - r_{ij}) \frac{\partial ((d_i + d_j)/2 - r_{ij})}{\partial \mathbf{r}_i} \\ &= -k^n \max(0, (d_i + d_j)/2 - r_{ij}) \frac{\mathbf{r}_{ij}}{r_{ij}} \\ &= -k^n \boldsymbol{\delta}_{ij}^n \mathbf{n}_{ij}, \end{aligned} \quad (68)$$

where we used the fact that $\max(0, (d_i + d_j)/2 - r_{ij})$ is continuous in time.

Further, we take the derivative $\partial_{r_{ia}} \boldsymbol{\delta}_{ij}^t$ (a denotes the vector coordinate) by the chain rule and use (9) to show that

$$\begin{aligned} \frac{\partial \boldsymbol{\delta}_{ij}^t}{\partial r_{ia}(t)} &= \frac{\partial t}{\partial r_{ia}(t)} \cdot \frac{\partial \boldsymbol{\delta}_{ij}^t}{\partial t} \Bigg|_{\mathbf{v}_j = \boldsymbol{\omega}_j = \mathbf{0}, v_{ib} = 0, b \neq a} \\ &= \frac{1}{v_{ia}} \cdot \left(v_{ia} \boldsymbol{\epsilon}_a + (-v_{ia} \boldsymbol{\epsilon}_a \cdot \mathbf{n}_{ij}) \mathbf{n}_{ij} + (\boldsymbol{\delta}_{ij}^t \cdot (-v_{ia} \boldsymbol{\epsilon}_a)) \frac{\mathbf{r}_{ij}}{r_{ij}^2} \right) \\ &= \boldsymbol{\epsilon}_a - n_{ija} \mathbf{n}_{ij} - \delta_{ija}^t \frac{\mathbf{r}_{ij}}{r_{ij}^2}, \end{aligned} \quad (69)$$

where $\boldsymbol{\epsilon}_a$ denotes the a -th basis vector of the coordinate system. Here, (69) becomes

$$\begin{aligned} \frac{\partial}{\partial r_{ia}} \frac{k^t}{2} \boldsymbol{\delta}_{ij}^{t2} &= k^t \boldsymbol{\delta}_{ij}^t \cdot \frac{\partial \boldsymbol{\delta}_{ij}^t}{\partial r_{ia}} \\ &= k^t \boldsymbol{\delta}_{ij}^t \cdot \left(\boldsymbol{\epsilon}_a - n_{ija} \mathbf{n}_{ij} - \delta_{ija}^t \frac{\mathbf{r}_{ij}}{r_{ij}^2} \right) \\ &= k^t \boldsymbol{\delta}_{ij}^t \cdot \boldsymbol{\epsilon}_a = k^t \delta_{ija}^t, \end{aligned} \quad (70)$$

where the cancellation of terms arises because the tangential spring is orthogonal to the normal vector. After substituting (70) and (68) into (67) we obtain

$$\begin{aligned} \frac{\partial H}{\partial \mathbf{r}_i} &= \frac{\partial}{\partial \mathbf{r}_i} \left(-m_i \mathbf{r}_i \cdot \mathbf{g} + \sum_{j \neq i} \frac{k^n}{2} |\boldsymbol{\delta}_{ij}^n|^2 + \frac{k^t}{2} |\boldsymbol{\delta}_{ij}^t|^2 \right) \\ &= -m_i \cdot \mathbf{g} - \sum_{j \neq i} k^n \boldsymbol{\delta}_{ij}^n \mathbf{n}_{ij} - k^t \boldsymbol{\delta}_{ij}^t = -\frac{d\mathbf{p}_i}{dt}. \end{aligned} \quad (71)$$

Next, we calculate

$$\frac{\partial H}{\partial \boldsymbol{\alpha}_{ia}} = \frac{\partial}{\partial \boldsymbol{\alpha}_{ia}} \sum_{j \neq i} k^t / 2 |\boldsymbol{\delta}_{ij}^t|^2 = \sum_{j \neq i} k^t \boldsymbol{\delta}_{ij}^t \cdot \frac{\partial}{\partial \boldsymbol{\alpha}_{ia}} \boldsymbol{\delta}_{ij}^t. \quad (72)$$

We take the derivative $\partial_{\boldsymbol{\alpha}_{ia}(t)} \boldsymbol{\delta}_{ij}^t$ using the chain rule and equations (9) and (8)

$$\begin{aligned} \frac{\partial \boldsymbol{\delta}_{ij}^t}{\partial \boldsymbol{\alpha}_{ia}(t)} &= \frac{\partial t}{\partial \boldsymbol{\alpha}_{ia}(t)} \frac{\partial \boldsymbol{\delta}_{ij}^t}{\partial t} \Bigg|_{\mathbf{v}_i = \mathbf{v}_j = \boldsymbol{\omega}_j = \mathbf{0}, \omega_{ib} = 0, b \neq a} \\ &= \frac{\partial t}{\partial \boldsymbol{\alpha}_{ia}(t)} \frac{\partial (-\boldsymbol{\omega}_i \boldsymbol{\epsilon}_a \times \mathbf{b}_{ij})}{\partial t} \Bigg|_{\mathbf{v}_i = \mathbf{v}_j = \boldsymbol{\omega}_j = \mathbf{0}, \omega_{ib} = 0, b \neq a} \\ &= -\boldsymbol{\epsilon}_a \times \mathbf{b}_{ij}. \end{aligned} \quad (73)$$

Substituting (73) into (72) we obtain

$$\frac{\partial H}{\partial \boldsymbol{\alpha}_{ia}} = -\sum_{j \neq i} k^t \boldsymbol{\delta}_{ij}^t \cdot (\boldsymbol{\epsilon}_a \times \mathbf{b}_{ij}) = \sum_{j \neq i} (k^t \boldsymbol{\delta}_{ij}^t \times \mathbf{b}_{ij})_a, \quad (74)$$

where we used the identity

$$\mathbf{c} \cdot (\boldsymbol{\epsilon}_a \times \mathbf{d}) = -(\mathbf{c} \times \mathbf{d})_a \quad \forall \mathbf{c}, \mathbf{d} \in \mathbb{R}^3. \quad (75)$$

Thus, using (72) and that \mathbf{b}_{ij} and \mathbf{n}_{ij} are parallel, we obtain

$$\frac{\partial H}{\partial \boldsymbol{\alpha}_i} = -\sum_{j \neq i} (\mathbf{b}_{ij} \times k^t \boldsymbol{\delta}_{ij}^t) = \sum_{j \neq i} (\mathbf{b}_{ij} \times \mathbf{f}_{ij}) = -\frac{d\boldsymbol{\phi}_i}{dt}. \quad (76)$$

Subsequently, we derive (66b) since

$$\frac{\partial H}{\partial \mathbf{p}_i} = \frac{\partial}{\partial \mathbf{p}_i} \frac{|\mathbf{p}_i|^2}{2m_i} = \frac{\mathbf{p}_i}{m_i} = \frac{d\mathbf{r}_i}{dt}, \quad (77)$$

and

$$\frac{\partial H}{\partial \boldsymbol{\phi}_i} = \frac{\partial}{\partial \boldsymbol{\phi}_i} \frac{\phi_i^2}{2I_i} = \frac{\phi_i}{I_i} = \frac{d\boldsymbol{\alpha}_i}{dt}. \quad (78)$$

Finally, we show that the total energy is conserved. Since mass m_i , radius r_i and spring constants k^n , k^t are constant, H has no direct dependence on t and thus

$$\frac{\partial H}{\partial t} = 0. \quad (79)$$

Using and (66) and (79) yields

$$\begin{aligned} \frac{d}{dt} H(t, \mathbf{r}, \mathbf{P}) &= \frac{\partial H}{\partial t} + \sum_{i=1}^N \frac{\partial H}{\partial \mathbf{r}_i} \cdot \frac{d\mathbf{r}_i}{dt} + \frac{\partial H}{\partial \boldsymbol{\alpha}_i} \cdot \frac{d\boldsymbol{\alpha}_i}{dt} + \frac{\partial H}{\partial \mathbf{p}_i} \cdot \frac{d\mathbf{p}_i}{dt} + \frac{\partial H}{\partial \boldsymbol{\phi}_i} \cdot \frac{d\boldsymbol{\phi}_i}{dt} \\ &= \frac{\partial H}{\partial t} - \frac{d\mathbf{p}_i}{dt} \cdot \frac{d\mathbf{r}_i}{dt} - \frac{d\boldsymbol{\phi}_i}{dt} \cdot \frac{d\boldsymbol{\alpha}_i}{dt} + \frac{d\mathbf{r}_i}{dt} \cdot \frac{d\mathbf{p}_i}{dt} + \frac{d\boldsymbol{\alpha}_i}{dt} \cdot \frac{d\boldsymbol{\phi}_i}{dt} \\ &= 0, \end{aligned} \quad (80)$$

Fig. 17 shows the energy balance of two particles colliding non-collinear in the dissipation- and yield-free case. One can see the jump in energy at the end of contact, where potential tangential spring energy is converted into internal energy.

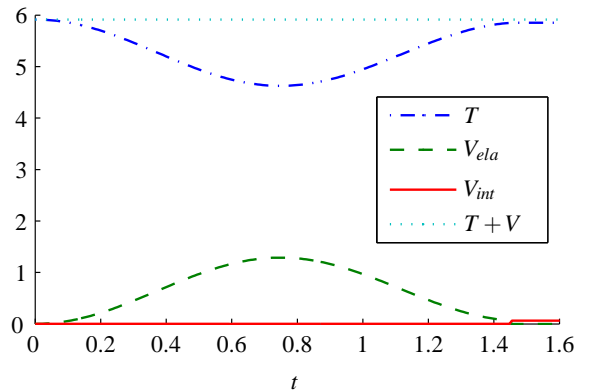


Fig. 17: Energy balance of two particles colliding non-collinear in the dissipation- and yield-free case. The kinetic and elastic potential energy are in balance, until the particles loose contact and potential spring energy is converted into internal energy.

B Orthogonality of the tangential spring

To show that the tangential spring is orthogonal to \mathbf{r}_{ij} , note that the tangential spring is initially of zero length and therefore orthogonal to \mathbf{r}_{ij} ; further

$$\begin{aligned} \frac{d(\delta_{ij}^t \cdot \mathbf{r}_{ij})}{dt} &= \frac{d\delta_{ij}^t}{dt} \cdot \mathbf{r}_{ij} + \delta_{ij}^t \cdot \mathbf{v}_{ij} \\ &= \left(\mathbf{v}_{ij}^t - \frac{(\delta_{ij}^t \cdot \mathbf{v}_{ij})\mathbf{r}_{ij}}{r_{ij}^2} \right) \cdot \mathbf{r}_{ij} + \delta_{ij}^t \cdot \mathbf{v}_{ij} \\ &= \mathbf{v}_{ij}^t \cdot \mathbf{r}_{ij} = 0 \end{aligned} \quad (81)$$

Thus, we can integrate equation (81) to obtain a continuously orthogonal tangential spring with $\delta_{ij}^t \cdot \mathbf{r}_{ij} = 0$.

C Algorithms for time integration and the calculation of the tangential force

The algorithm for the time integration and the calculation of the tangential force is shown in Algorithms 1 and 2.

Algorithm 1: Time integration

Data: Initial positions and translational and angular velocities

$\mathbf{r}_i^0, \mathbf{v}_i^0, \boldsymbol{\omega}_i^0$, masses m_i , inertias I_i , time step Δt

$\mathbf{r}_i \leftarrow \mathbf{r}_i^0, \mathbf{v}_i \leftarrow \mathbf{v}_i^0, \boldsymbol{\omega}_i \leftarrow \boldsymbol{\omega}_i^0 \forall i$

$(\mathbf{f}_i, \mathbf{q}_i) \leftarrow \text{forces-and-torques}(\{\mathbf{r}_j, \mathbf{v}_j, \boldsymbol{\omega}_j\}_{j=1}^N) \forall i$

for $i = 1, 2, \dots, N$ **do**

$\mathbf{v}_i \leftarrow \mathbf{v}_i + \frac{\Delta t}{2} \frac{\mathbf{f}_i}{m_i} \forall i$

$\boldsymbol{\omega}_i \leftarrow \boldsymbol{\omega}_i + \frac{\Delta t}{2} \frac{\mathbf{q}_i}{I_i} \forall i$

$\mathbf{r}_i \leftarrow \mathbf{r}_i + \Delta t \mathbf{v}_i \forall i$

foreach particle pair (i, j) **in contact** **do**

if contact is new **then** $\delta_{ij}^t \leftarrow \mathbf{0}$

$\mathbf{a}_{ij}^t \leftarrow \mathbf{v}_{ij}^t - \frac{(\delta_{ij}^t \cdot \mathbf{v}_{ij})\mathbf{r}_{ij}}{r_{ij}^2}$

$\delta_{ij}^t \leftarrow \delta_{ij}^t + \Delta t \mathbf{a}_{ij}^t$

$(\mathbf{f}_i, \mathbf{q}_i) \leftarrow \text{forces-and-torques}(\{\mathbf{r}_j, \mathbf{v}_j, \boldsymbol{\omega}_j\}_{j=1}^N) \forall i$

$\mathbf{v}_i \leftarrow \mathbf{v}_i + \frac{\Delta t}{2} \frac{\mathbf{f}_i}{m_i} \forall i$

$\boldsymbol{\omega}_i \leftarrow \boldsymbol{\omega}_i + \frac{\Delta t}{2} \frac{\mathbf{q}_i}{I_i} \forall i$

Algorithm 2: Calculation of the tangential force, including sliding

$\mathbf{f}_{ij}^t \leftarrow -k^t \delta_{ij}^t - \gamma^t \mathbf{v}_{ij}^t$

if $(|\mathbf{f}_{ij}^t| > \mu_c |\mathbf{f}_{ij}^n|)$ **then**

$\mathbf{f}_{ij}^t \leftarrow \mu_c \frac{|\mathbf{f}_{ij}^n|}{|\mathbf{f}_{ij}^t|} \mathbf{f}_{ij}^t$

$\delta_{ij}^t \leftarrow -\frac{1}{k^t} (\mathbf{f}_{ij}^t + \gamma^t \mathbf{v}_{ij}^t)$
